Robust Clustering of the Local Milky Way Stellar Kinematic Substructures with *Gaia* eDR3

Xiaowei Ou (欧筱葳),[1] Lina Necib,[1, 2] and Anna Frebel[1]

[1]*Kavli Institute for Astrophysics and Space Research, Massachusetts Institute of Technology, 77 Massachusetts Ave, Cambridge MA 02139, USA*

[2]*The NSF AI Institute for Artificial Intelligence and Fundamental Interactions, Massachusetts Institute of Technology, 77 Massachusetts Ave, Cambridge MA 02139, USA*

ABSTRACT

We apply the clustering algorithm `HDBSCAN` on the *Gaia* early third data release astrometry combined with the *Gaia* second data release radial velocity measurements of almost 5.5 million stars to identify the local stellar kinematic substructures in the solar neighborhood. Understanding these structures helps build a more complete picture of the formation of the Milky Way, as well as an empirical phase space distribution of dark matter that would inform detection experiments. The main goal of this study is to provide a list of the most stable clusters, by taking into account the measurement uncertainties and studying the stability of the clustering results. We apply the clustering algorithm in two spaces, in velocity space in order to study recently accreted structures, and in action-angle space to find phase-mixed structures. We find 1405 (497) stars in 23 (6) robust clusters in velocity space (action-angle space) that are consistently not associated with noise. They are attributed to the known structures: the Gaia Sausage-Enceladus, the Helmi Stream, and globular cluster NGC 3201 are found in both spaces, while NGC 104 and the thick disk (Sequoia) are identified in velocity space (action-angle space). We discuss the kinematic properties of these structures, and cross match them with APOGEE DR17 and LAMOST DR6 to study whether many of the small clusters belong to a similar larger cluster based on their chemical abundances. Although we do not identify any new structures, we find that the `HDBSCAN` member selection of already known structures is unstable to input kinematics of the stars when resampled within their uncertainties. We therefore present the most stable subset of local kinematic structures, which are consistently identified by the clustering algorithm, and emphasize the need to take into account error propagation during both the manual and automated identification of stellar structures, both for existing ones as well as future discoveries.

Keywords: Galactic archaeology — Milky Way dynamics — Milky Way dark matter halo

1. INTRODUCTION

In the most popular cosmological structure formation model, typical spiral galaxies, like our Milky Way, form hierarchically through many mergers with less massive galaxies (see e.g. White & Rees 1978; Frenk & White 2012; Wechsler & Tinker 2018; Behroozi et al. 2019). Theories and simulations predict that most of the merging stellar populations are tidally disrupted during infall, and form various structures in today's Milky Way stellar halo (Zolotov et al. 2009; Cooper et al. 2010). These accreted stars appear in large all-sky surveys as spatially coherent kinematic structures ("streams"), as well as mere overdensities in orbital energy and angular momenta after phase mixing ("tidal debris") (for a review see e.g., Helmi (2020)). Studying these accreted stars allows us to estimate properties of their progenitors (e.g., mass, age, infall time, and kinematics). The stellar chemical signatures of such structures, such as metallicity and α-element abundances (Freeman & Bland-Hawthorn 2002; Frebel & Norris 2015; Maiolino & Mannucci 2019; Sestito et al. 2019; Fattahi et al. 2020), and kinematic properties (Johnston et al. 1996; Johnston 1998; Helmi et al. 1999; Bullock & Johnston 2005; Johnston et al. 2008) thus provide unique information about the formation history of the Milky Way.

Understanding the merger history of the Milky Way and the properties of the accreted and merged progenitors galaxies can help us learn about near-field cosmology and provide constraints on structure formation and galaxy evolution in the late time universe (see e.g., Myeong et al. (2019); Mackereth et al. (2019); Belokurov et al. (2020); Feuillet et al. (2022)). At the same time, Herzog-Arbeitman et al. (2018a,b); Necib et al. (2019a) found that the stellar component of the accreted sys-

Email: xwou@mit.edu

tems may be used as a tracer of the accompanying dark matter (DM) accreted along with the system. The DM distribution in the Milky Way, especially near the solar neighborhood, is one of the key ingredients towards uncovering the particle nature of DM. Direct detection rates of DM particles rely on the proper modeling of the local DM density and velocity distributions, which translates discoveries as well as null results into a DM mass and DM-nucleon scattering cross section (Goodman & Witten 1985; Drukier et al. 1986; Jungman et al. 1996).

Using accreted stars to answer near-field cosmology questions and as DM tracers relies on efficiently and accurately identifying them in the local solar neighborhood. Since our solar system resides in the thin disk of the Milky Way, the local stellar population is dominated by in-situ stars formed in the thin disk (Soubiran et al. 2003). Thus, while earlier discoveries and studies (see e.g., Ibata et al. (1994); Belokurov et al. (2006); Schlaufman et al. (2009)) were carried out with chemical abundance measurements and small kinematic data sets, identifying some of the more elusive accreted stellar populations, such as Thamnos and the metal-weak Atari disk, on top of this in-situ background relies on obtaining 6D kinematic information for a large data set of local stars. Large kinematics data sets are powerful in identifying intact satellites that are in the early stage of accretion, diffuse satellites that have phase-mixed into the environment, as well as those that are in the process of transitioning from the former to the latter via tidal disruption. This can now be done with large photometric and astrometric surveys such as the *Gaia* mission (Gaia Collaboration et al. 2016, 2018, 2021).

Many studies have already used these data to identify numerous substructures that merged into the Milky Way in the past (Belokurov et al. 2018; Helmi et al. 2018; Myeong et al. 2018; Koppelman et al. 2019a; Necib et al. 2019a; Helmi 2020). Among these local structures, the Gaia-Enceladus/Sausage (GSE) is the most recent major merger event experienced by the Milky Way (Belokurov et al. 2018; Helmi et al. 2018). Additionally, Koppelman et al. (2019a) discovered the Thamnos structure in the *Gaia* second data release (DR2) as part of the local retrograde halo. Sequoia, a high energy retrograde structure originally attributed to being part of the GSE by Helmi et al. (2018), was found to be most likely coming from a separate accretion event in Myeong et al. (2019) with *Gaia* DR2 data. Sharing similar kinematic properties, Arjuna and I'itoi were discovered in Naidu et al. (2020) as distinct accretion debris given their metallicity differences after combining data from the *Gaia* DR2 and the H3 survey(Gaia Collaboration et al. 2018; Conroy et al. 2019). Wukong and Aleph, two prograde structures, were found similarly by Naidu et al. (2020): Aleph is a highly prograde structure with circular orbits and a significant vertical motion, as well as a metal-rich and relatively alpha-poor chemistry. Wukong

is also a prograde structure lining the margin of the GSE in the E_{tot} *vs.* L_z plane, shown as two over-densities at $E_z \sim -1.1$ and $-1.3 \times 10^5 \, \mathrm{km^2 \, s^{-2}}$. Spatially coherent streams such as S1, Icarus, and Nyx, to name a few, are also identified (Myeong et al. 2018; Meingast et al. 2019; Re Fiorentin et al. 2020). They are associated to either past merger events or disk clusters.

Past discoveries of local over-densities such as the Helmi stream (Helmi & White 1999) have also been further studied with *Gaia* data (Koppelman et al. 2019b). The long known "metal weak thick disk" (Norris et al. 1985; Morrison 1990; Chiba & Beers 2000) has recently been postulated to be likely the result of a merger, rather than part of the canonical thick disk. Mardini et al. (2022) confirmed such origin with photometric metallicities from the SkyMapper survey (Keller et al. 2007; Wolf et al. 2018; Chiti et al. 2021) and kinematics from *Gaia* . Using machine learning techniques trained on simulations (Wetzel et al. 2016; Hopkins et al. 2018; Sanderson et al. 2020), and labeling the *Gaia* DR2 data set, Ostdiek et al. (2020) built an accreted star catalog (Ostdiek et al. 2019) from which multiple structures were identified (Necib et al. 2020a), including Nyx (Necib et al. 2020b), a stream within the thick disk with a highly eccentric orbit.

These studies use the fact that accreted substructures emerge as overdensities in the 6D phase space. The key, thus, is extracting such overdensities effectively and robustly from the data. Current studies mostly rely on two main methods in identifying overdensities and selecting their constituents: manual selection (Helmi et al. 2018; Lee et al. 2019; Naidu et al. 2020; Carollo & Chiba 2021) and clustering algorithms (Helmi et al. 2017; Necib et al. 2019a,b; Yang et al. 2019; Wu et al. 2022; Sofie Lövdal et al. 2022), or some combination of both (Koppelman et al. 2019a; Bird et al. 2021) (see Buder et al. (2022) Table A.1 for a review of techniques).

For manual selection, overdensities in phase space are identified based on physical intuition gained from past discoveries (Naidu et al. 2020) or statistical comparisons with some reference random data set (Helmi et al. 2018). They are then characterized based on their phase space properties. Potential background contamination is removed by examining stellar population properties, such as age and metallicity distributions. This method relies on the fact that an overdensity is located in phase space where the background contamination level is low, either because the substructures themselves have peculiar properties which set them apart from the majority of the in-situ Milky Way stars, or because astronomers are able to apply well-informed cuts on the data set to remove most of the background. For structures that reside within or close to the Milky Way background, manual selection becomes difficult and tricky.

For machine learning-focused methods, structures are picked out directly from the data sample with minimum preprocessing by various algorithms. The results are,

in general, more consistent between works, for example, especially when using the same algorithm. Naturally, this is not frequently true for manual selections. In most cases, however, the final results need to be further examined, combined with additional less complete information such as metallicity and chemical abundances, to remove unphysical structures such as background noise and data artifacts. Brauer et al. (2022) tested kinematic-based clustering algorithms on simulations and showed that they generally lack efficiency and accuracy in identifying structures resulting from now-dissolved ultra faint dwarf galaxies.

Despite the difficulties mentioned above, both methods have yielded many new structures in the solar neighborhood that have been extensively studied and validated. Yet, it is still often the case that the stellar membership of any of these structures has to be confirmed with archive/follow-up spectroscopic observations if they were initially discovered based on kinematic information only. Even with the best informed physical expectation and/or the most sophisticated algorithms, the kinematic selection alone is typically not enough to robustly determine the constituent stars, even when the overdensities/structures are principally well-established. This is due not only to the background-dominated signal search (i.e., the in-situ population) but also, and more importantly, due to our inability to measure the stellar kinematics infinitely precisely. Despite the recent advancement in astrometric survey precision, uncertainties still play a large role that affects stellar membership assignments. For practical reasons, uncertainties are often left out in kinematic structure studies, either because the machine learning algorithm inherently does not support uncertainties or because the process becomes too computationally intensive. This lack continues to hamper the robustness of identifying additional structures to eventually identify all progenitors of the Milky Way.

In this paper, we aim to incorporate uncertainties for the first time into an unsupervised machine learning algorithm to search for Milky Way substructures in *Gaia*. The goal is to select a robust sample of star members present in clusters/overdensities purely based on kinematic inputs. We use the Hierarchical Density-Based Spatial Clustering of Applications with Noise (`HDBSCAN`) (McInnes et al. 2017), an unsupervised learning algorithm, to identify clusters in the 6D phase space with data from the *Gaia* eDR3 data set (Gaia Collaboration et al. 2021). We combine Monte Carlo resampling and Jaccard coefficients to estimate the robustness of the `HDBSCAN` clusters. Doing so currently leads us to identify only the most robust clusters and their member stars. We recover the GSE, Sequoia, the Helmi Stream, and globular clusters NGC 3201 and NGC 104, but do not Thamnos and Nyx due to an initial cut on the maximum orbital vertical distance $Z_{\max}$, or Arjuna and I'itoi which could be a subset of Sequoia in our analysis, or Aleph and Wukong that we expect to be either unsta-

ble, or dominant further away from the disk than our sample. Our results demonstrate the importance of incorporating uncertainties in machine learning, especially unsupervised clustering, for astronomy studies, and how this approach affects our interpretation of the clustering results and the constituent stars within the clusters.

This paper is structured as follows: We discuss the data sample used for this study in Section 2. The clustering algorithm is discussed in Section 3. We present the clustering results in Section 4 and discuss their interpretations in Section 5.

2. DATA SET

2.1. *Quality Cuts*

We first apply quality cuts on *Gaia* eDR3 stars, combined with the radial velocity measurements from *Gaia* DR2. Based on recommendations from Lindegren et al. (2021a), we select sources with good astrometric solutions by requiring `parallax_over_error > 5`, `ruwe < 1.4`, `astrometric_excess_noise < 2`, `duplicated_source = 0`, $G < 19$, and `visibility_periods_used >= 10`. We also perform the cut on color `C = phot_bp_rp_excess_factor` with the prescription described by Riello et al. (2021) to remove faint sources in close proximity to bright sources. We then correct for the zero point bias in the parallaxes as described in Lindegren et al. (2021b).

The data sample size, after applying the quality cuts mentioned above, and removing high-velocity stars ($|v_i| > 1000$ km s^{-1} where $i = r, z, \phi$), is 5,557,670. More cuts are applied to the sample before going through the clustering algorithm, which are described in the following sections.

2.2. *Crossmatched Data Sets*

For extra chemical information, we crossmatch the sample with the spectroscopic surveys LAMOST DR6 (632,223 matches) (Cui et al. 2012; Zhao et al. 2012) and APOGEE DR17 (211,798 matches) (Majewski et al. 2017; Abdurro'uf et al. 2022). We focus mainly on the metallicity measurements from these two surveys, as LAMOST provides the most matching sources and APOGEE provides the most α-abundances.

Chemical abundance information is used for characterization of individual clusters, comparison between clusters, and comparison with literature. To avoid systematic differences across data sets, we limit metallicity characterizations of our identified clusters to one survey at any given time. Unless otherwise noted, we use APOGEE metallicities and α abundances in summary plots for characterizing individual clusters as APOGEE chemical abundances are derived from high-resolution spectra than those from LAMOST (medium-resolution spectra only). However, for examining relationships between the final clusters in this study and for a comparison with known structures' metallicities from the

literature, we instead use metallicities from LAMOST
that are available for more of our cluster stars and thus
provide better statistics. We discuss more details in Sec-
tion 5.

2.3. Z_{max} Cuts

It is extremely difficult, if not impossible, for most
clustering algorithms to identify substructure signals
over a strong background. The majority of our sam-
ple is made up of in-situ thin disk stars, which, if not
removed in some way, will flood all signals and prevent
detecting any meaningful clustering. To remove the thin
disk contamination, a standard practice in the field has
been to perform a velocity cut in the local standard of
rest (LSR) velocity (see e.g., Helmi et al. (2018); Sofie
Lövdal et al. (2022)). Where spectral information is
available, velocity cuts are also combined with metallic-
ity cuts to exclude metal-rich disk stars (see e.g., Myeong
et al. (2018)). This method is the most successful in
completely removing stars with thin disk-like kinemat-
ics, thus leaving behind a sample comprised primarily
of halo stars and some hot thick disk stars. However,
the disadvantages of this method are that it might bias
the overall velocity distribution of the resulting sam-
ple, or drop some of the prograde structures (e.g., Nyx
(Necib et al. 2020b)). Since our goal is to identify veloc-
ity structures and eventually their impact on the local
DM velocity distributions in future work, we here opt for
the least kinematically biased sample possible by instead
placing a Z_{max} cut rather than using a direct velocity
cut.

Specifically, we apply a cut at $Z_{max}> 2.5$ kpc to re-
move the thin disk, and to keep the possibility of study-
ing potential prograde structures with high vertical mo-
tion. The left panel of Fig. 1 shows the Toomre plot of
our initial sample, where stars in the thin disk ($V \sim 220$
$km\,s^{-1}$) dominate by orders of magnitude over the rest
of the stars, which would also include any prograde kine-
matic substructures.

Our Z_{max} is calculated through orbit integration, as
detailed in Section 2.5. We expect most in-situ stars to
have Z_{max} no higher than 2.5 kpc, especially with a thin
disk scale height approximately at 300 pc (Jurić et al.
2008). Thus, this cut will serve the purpose of remov-
ing the thin disk, similar to the LSR velocity cut, but at
the same time it will allow potential prograde structures
with high vertical motion to remain in the final sample.
As shown in Figure 2, the v_ϕ distribution of stars at
higher Z_{max} interval shows a clear transition from the
expected rotational velocity of the disk of -220 $km\,s^{-1}$
towards 0 $km\,s^{-1}$, the average rotational velocity of the
stellar halo. Figure 1 also indicates a significant portion
of the stars that would have been removed by an LSR
velocity cut (red dashed line) remaining in the post-cut
sample. Our Z_{max} cut is not as clean as a LSR veloc-
ity cut, by design, as even at vertical distances a few
times above the scale height of the thin disk, the expo-

nential tail of the thin disk is still comparable in size to
the slower rotating prograde halo, and retrograde halo
populations. Jurić et al. (2008) measured the local halo-
to-thin disk stellar number density ratio of 0.5%. In
addition to that, the uncertainty in our distance mea-
surements unavoidably creates a systematically puffed-
up thin disk, causing a significant amount of prograde
stars with kinematics very similar to that of the thin disk
even at Z_{max} greater than 3 kpc. Yet, doing so gives us
the opportunity to study potential overdensities in the
high vertical motion tail of the thin disk.

More specifically, in terms of potential velocity biases,
while this cut still poses an implicit bias on the distri-
bution of the velocity in the z direction, it is neverthe-
less much less restrictive than the LSR cut. Again, this
leaves space for prograde accreted stars to be part of
the clustering sample. Following this reasoning, we re-
quire $Z_{max}> 2.5$ kpc, as well as that the mean value
of Z_{max} has to be larger than two standard deviations
above the cut when taking into account the errors in the
measurements.

### 2.4. Coordinate Transformations

After sample selection, we compute the galactocentric
coordinates and velocities assuming the Astropy galac-
tocentric frame with default parameters adopted in As-
tropy v4.0 (Astropy Collaboration et al. 2013, 2018).
The galactic center coordinate is at ra=266.4051° and
dec=-28.936175°(Reid & Brunthaler 2004). The right-
handed coordinate system is defined such that the x-axis
points from the Sun to the galactic center and the y-axis
points in the direction of local disk rotation. The dis-
tance to the galactic center is assumed to be 8.122 kpc
(Gravity Collaboration et al. 2018), with the Sun mov-
ing with velocity (12.9, 245.6, 7.78) $km\,s^{-1}$ and located
20.8 pc above the midplane (Drimmel & Poggio 2018;
Bennett & Bovy 2019).

Uncertainties on the galactocentric velocities and po-
sitions are propagated from uncertainties in parallax,
proper motion, and radial velocities. We take into ac-
count covariances between Gaia measured parallax and
proper motions. As a result, there exist non-trivial co-
variances between the transformed galactocentric veloc-
ities, which we will take into account in the orbit inte-
gration. Radial velocities are measured from Gaia DR2
and have no provided covariances with other Gaia EDR3
astrometry measurements.

2.5. Orbit Integration

We integrate the orbits for our final sample backward
in time for 2.5 Gyr with 1 Myr steps using the Python
agama package (Vasiliev 2019). We set up the potential
to be the default MilkyWayPotential from GALA v1.4.1,
which is a four-component potential model consisting of
a bulge and nucleus with Hernquist profile Hernquist
(1990), a disk with Miyamoto-Nagai profile Miyamoto
& Nagai (1975), and a halo following the NFW profile
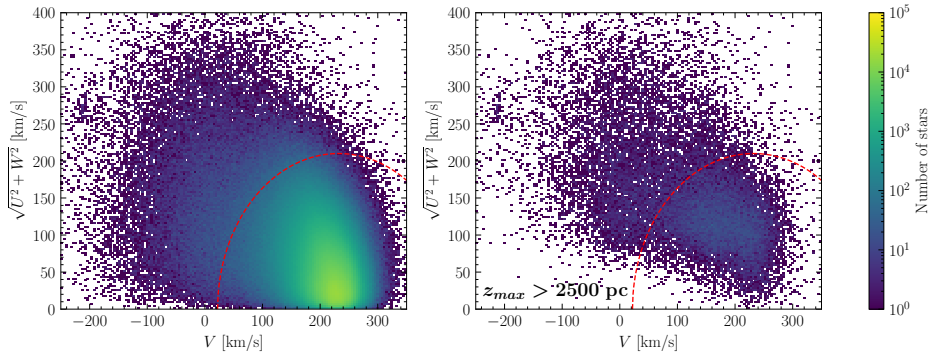
Figure 1. Toomre plots for the full sample (left) and the subsample with Z_{max} cut at 2500 pc, as indicated at the bottom-left of each panel. The red dashed line indicates a probable LSR velocity cut at 210 km s^{-1}, with $V_{LSR} = 232$ km s^{-1}.
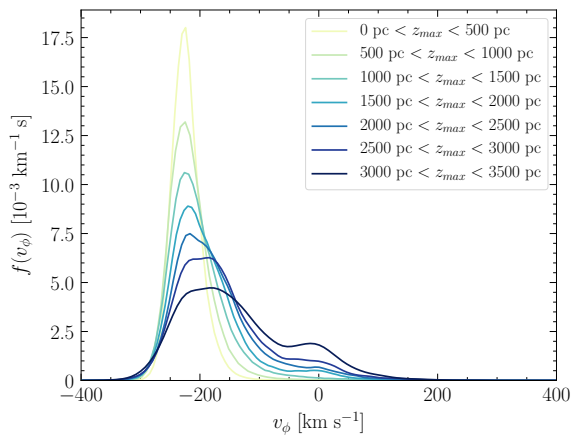
Figure 2. Normalized distribution of v_ϕ for increasing Z_{max} intervals, including only stars with available *Gaia* 2 RV. The v_ϕ histogram was constructed from bins between 0 to 3.5 kpc, in 500 pc intervals. There is a gradual shift in the overall distribution away from the LRS at ~ -220 km s^{-1} towards 0 km s^{-1}, as the sample evolves from thin-disk dominated to halo dominated.

Navarro et al. (1997). The disk model is taken from Bovy (2015) and the rest are fixed by fitting to a compilation of mass measurements of the Milky Way. More details on the parameters can be found in the GALA documentation (Price-Whelan 2017). Orbital parameters including energy, angular momenta, eccentricity, maximum galactic Z_{max}, apogalacticon, perigalacticon, and actions are derived from the integrated orbits.

For each star, we estimate the uncertainties for the orbital parameters by resampling the initial positions and velocities 100 times with their respective uncertainties (assuming the uncertainties are inherently Gaussian) and including the covariances between the velocities. Actions are calculated using the `ActionFinder` routine provided by `agama`. We note that while their effect is minimal, we include the covariance between the positions and velocities to compute the uncertainties in the orbital parameters. We then record the mean and standard deviation of these parameters as the final values and corresponding uncertainties.

3. CLUSTERING ALGORITHM

The main goal of this study is to identify kinematic clusters, from machine learning algorithms, which are stable under resampling within the uncertainties of the stellar kinematics inputs. Our method thus focuses on ensuring that the members of the extracted clusters are stable against being assigned as noise or as parts of different clusters as can occur when uncertainties are not taken into account. Consequently, stars we assign as cluster members are very stable against any splitting/merging of their apparent host clusters; splitting refers to a cluster breaking into smaller clusters, and merging refers to multiple clusters merging into one single cluster.

Given the complexity of this section, we summarize the main points here. We apply the clustering algorithm `HDBSCAN` (defined with its parameters in Section 3.1) on two separate spaces: The 3-dimensional cylindrical velocity space, and the 3-dimensional action space with total energy as an additional axis (see Section 3.2). In order to incorporate the uncertainties, we first define a high-stability sample by only selecting the stars that get clustered more than N_{stack}^{cut} times (defined in Section 3.4) when applying `HDBSCAN` over 100 realizations, as shown in Section 3.3. We then cluster the high-stability stars, and define the Jaccard coefficient as a measure of the stability of clusters (Section 3.5).

3.1. *Choice of Algorithm*

We adopt HDBSCAN[1] as a clustering algorithm for identifying the kinematic substructures in the *Gaia* data (McInnes et al. 2017). The choice of the clustering algorithm depends on the particularity of the data set. Specifically, we do not know a prior total number of clusters, the clusters could be of various shapes, and the data inherently has stars that are not part of a cluster, and would therefore need to be treated as noise. Ideally, the required algorithm would address the specifics of the data above, and potentially it would incorporate measurement uncertainties. Given the difficulty in finding an algorithm that has a standard treatment of measurement errors, a stability study of the resulting clusters is required, as we will discuss in Section 3.5.

HDBSCAN stands out to be the most ideal choice for our study. The algorithm transforms the space according to the density of points, and performs single linkage clustering on the transformed space. HDBSCAN assumes dense regions as clusters and thus makes no assumption about the intrinsic distribution or total number of clusters. It also does not require every data point to be assigned to a cluster, allowing the presence of noise. It builds a merger tree, where one can cut at variable heights to decide the smallest sized cluster based on a few hyperparameters, mostly min_cluster_size, which determines whether a split of the tree should be treated as two new clusters or one cluster losing noise points. The resulting clusters can thus have varying densities as long as they are stable against further splitting. Additionally, the clusters found are deterministic with the same input data and hyperparameters setting. Brauer et al. (2022) examined the performance of a suite of clustering algorithms on the Caterpillar cosmological simulation (Griffen et al. 2016) while trying to recover substructures left behind by accreted ultra-faint dwarf galaxies. Their result demonstrates that HDBSCAN has the best performance among all algorithms, albeit not powerful enough to identify all subtle, long-accreted clusters.

The parameters of the algorithm are set to default with the exception of min_cluster_size, which is set to 20 to capture the smallest substructure, and cluster_selection_method, which is set to leaf to track the leaf nodes of the clustering tree. As described in Section 3.5, the merging of these smaller homogeneous clusters along the hierarchical tree can be altered significantly due to uncertainties. Instead of having HDBSCAN decide how the leaf nodes should be merged, it is more consistent to first examine the stability of the leaf nodes individually (and how they change with uncertainties folded in), as shown in Section 3.5. We then considered separately if and how they may be merged, as shown in Section 4.3.

3.2. *Clustering Spaces*

In this work, we apply HDBSCAN to two separate spaces: The 3-dimensional cylindrical velocity space and the 3-dimensional action space with total energy as an additional axis. First, the cylindrical velocity clustering space is chosen as it will identify stellar kinematic substructures, which might correlate with DM velocity substructures. As shown in Necib et al. (2019b), the stellar velocity distribution of debris flows would be correlated with the velocity distribution of DM, which is key in studying DM direct detection rates.

Second, we also perform clustering in the integrals of motion space for accreted structures that have phase-mixed since their accretion. In particular, we perform clustering on the total energy and the 3D action space. Previous works have discussed the fact that accreted stellar populations remain clustered in such integral of motion space long after the merger, given a slowly varying potential, from both theory (Binney & Spergel 1982) and simulation (Helmi et al. 1999; Knebe et al. 2005; Gómez et al. 2010) perspectives. While these structures may no longer show a coherent velocity distribution, they are nonetheless important sources of accreted DM and would affect the local DM velocity distribution.

For the reasons mentioned above, we do not expect a one-to-one correspondence between the clusters identified in one space and those from the other. Nonetheless, we compare the clustering results from these two spaces in Section 4 as these results complement each other. Moreover, they allow us to study, in future work, the local DM velocity distribution from both coherent and phase-mixed accreted structures.

3.3. *Uncertainties: Random Realizations and Stacking*

HDBSCAN, similarly to most clustering algorithms, is not designed for handling data with uncertainties. Previous work (see e.g., Koppelman et al. 2019a) that had used HDBSCAN for cluster identification, did not take uncertainties into account when applying the algorithm to kinematic data. Other works have included measurement uncertainties on a much smaller scale, typically on the order of thousands of stars; for example, Limberg et al. (2021); Gudin et al. (2021); Shank et al. (2022) used HDBSCAN to identify dynamically tagged groups for very metal-poor stars. Limberg et al. (2021) proposed estimating the confidence level of the clusters via feeding Monte Carlo generated perturbed data sets into the HDBSCAN hierarchical tree generated from the nominal values. The cluster membership assignment is re-evaluated using the prediction method provided by the HDBSCAN package.[2] As pointed out by the authors of

---

[2] This procedure provides estimates on the probability of a given star being the member of a cluster, considering uncertainties on the kinematic properties, which indirectly evaluates the robustness of the clusters themselves. All probabilities are based on the hierarchical tree generated by HDBSCAN from the nominal (or mean) kinematic properties of the sample stars.

HDBSCAN, the algorithm is a transductive method, meaning new/perturbed data points can and should alter the underlying clustering (McInnes et al. 2017). This is especially the case if one attempts to predict the membership assignment of an entire perturbed data set with a size identical to the original nominal data set used to generate the tree. The membership assignments for the perturbed data sets are thus inherently inconsistent with the hierarchical tree.

In this work, we adopt a self-consistent method of simultaneously evaluating the robustness of the clusters themselves and the membership of the stars within the clusters by regenerating the hierarchical clustering tree for each Monte Carlo resampled data set. Specifically, uncertainties are incorporated by repeating the clustering process with input parameters resampled from their respective uncertainties for 100 times. We repeat the clustering procedure with 100 realizations, sampled from the error bars on each of the variables included. The clustering results from each random realization are then combined together in order to establish the stability of the clusters. We find that, while the general clustering results may appear similar by eye in various spaces, the exact stellar membership could differ significantly between realizations. Clusters that are in close proximity to other clusters often exchange members due to the existence of noise and background. Such behavior results in the clusters themselves shifting around in the clustering space, and sometimes merging and splitting between different realizations. It is thus extremely difficult to directly quantify the stability of the clusters.

To overcome this challenge, instead of directly evaluating the stability of individual clusters, we first focus our attention on the stars themselves. We stack the clustering results from all 100 realizations, and instead of recording the membership of the stars to specific clusters (or noise), we simply record whether or not the stars are identified to be part of some cluster at all. The result is a distribution of the number of times a given star is clustered to be non-noise. Stars that are consistently clustered can then be selected by making a cut on the number of times the star has been clustered; we call this variable N_{stack}. An $N_{\mathrm{stack}}^{\mathrm{cut}}$ allows us to identify the stable stars first, that are more often part of a cluster and not the noise, which can then be used to find the stable clusters. We call the sample of stars after this cut the high-stability sample.

The sample size of the high-stability sample is significantly smaller than the full sample. It does, however, guarantee that the clusters found in this sample

are much more robust with respect to any resampling of the kinematic inputs within their uncertainties. The fact that these stars are associated with some cluster in multiple random realizations signifies that these stars stay close to overdensities in the parameter space. More importantly, the overdensities themselves remain significant above the background such that HDBSCAN would identify them as clusters. We can think of this as deepening the contrast of the clustering space. We show these high-stability sample stars (in red) as well as the entire sample (in black) in Figure 3. Some structures are visible by eye in this high-stability sample.

3.4. Selection of $N_{\mathrm{stack}}^{\mathrm{cut}}$

We choose $N_{\mathrm{stack}}^{\mathrm{cut}}$=20 to balance sample sizes and overall stabilities of the final clusters. The sample size of the high-stability sample reduces as shown in Figure S1, while the stabilities of the final clusters improve with increasing $N_{\mathrm{stack}}^{\mathrm{cut}}$. We tested the clustering results' stabilities of high-stability samples using different $N_{\mathrm{stack}}^{\mathrm{cut}}$, following methods detailed in Section 3.5, and found that $N_{\mathrm{stack}}^{\mathrm{cut}}$ at 20 yields the largest sample of stable stars with most of the final clusters being stable.

We find no obvious correlation between the $N_{\mathrm{stack}}^{\mathrm{cut}}$ and the uncertainty distribution of the high-stability sample. A concern of the $N_{\mathrm{stack}}^{\mathrm{cut}}$ would be that it reduced the data size by essentially performing an uncertainty cut, biasing towards stars that do not move as much in the clustering space. To test this, we examine the uncertainty distribution of the subsample in 3D cylindrical velocity space with and without N_{stack} cut, shown in Figure S2. The result indicates a minimum effect on the overall distribution of the uncertainties in any of the cylindrical velocities. We are thus confident that the stars with lower N_{stack} are not excluded because of high uncertainties but because they are at the edge of the identified clusters in the clustering spaces. In other words, under the same level of uncertainties, they blend in with the background noise more easily given their position in the clustering space, and thus N_{stack} is selecting physically more significant stars as part of a cluster than just statistically better measured stellar kinematics. The same test is carried out in the integrals of motion space with a similar result.

After identifying the stable stars, we apply HDBSCAN with the same parameter settings on only the stars, with N_{stack} above 20. The resulting clusters on this high-stability sample are taken as the final clusters.
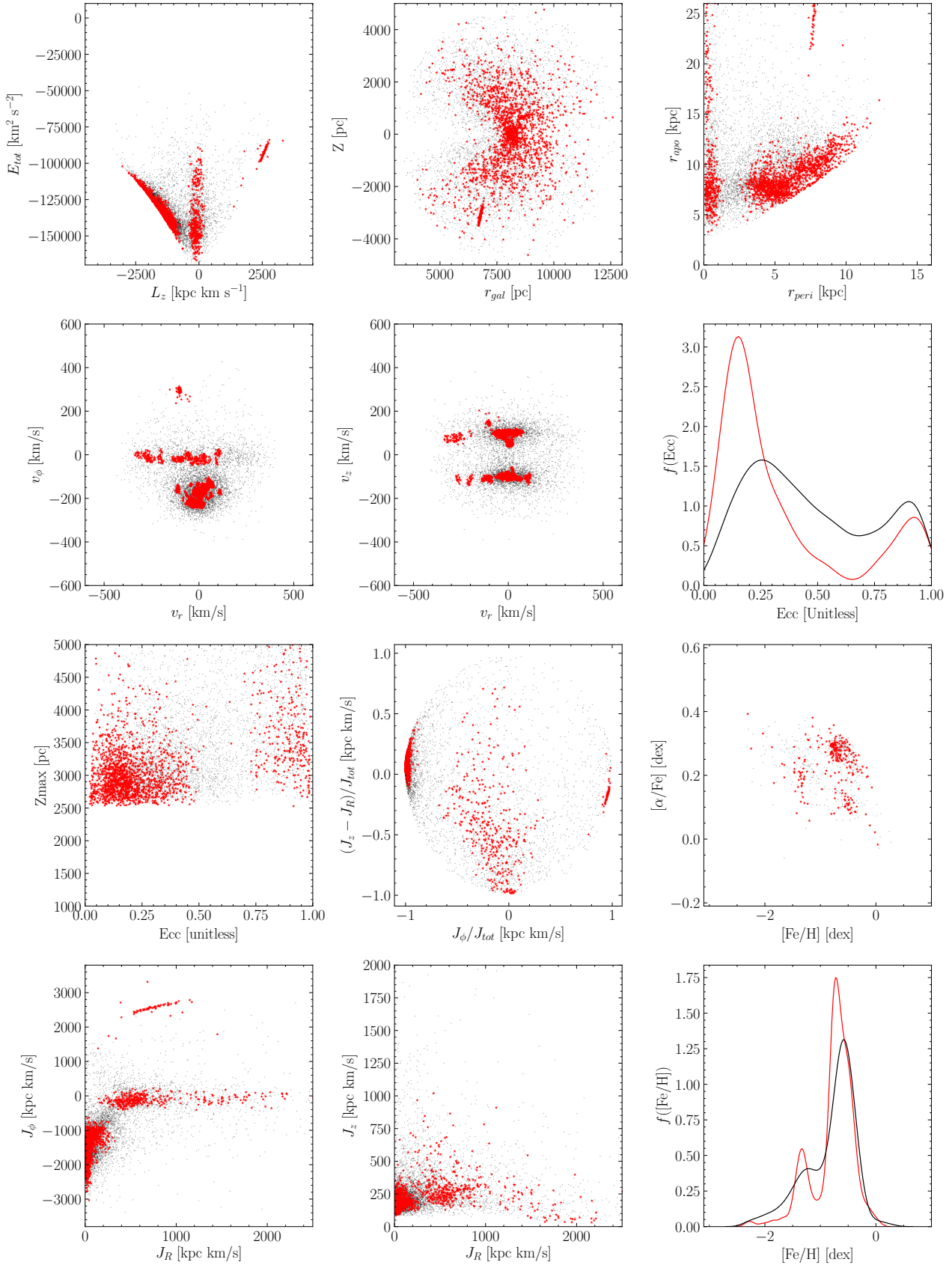
Figure 3. Summary plot for the full sample (black), downsampled to 20%, with the high-stability ($N_{\mathrm{stack}} > 20$) sample (red) identified from the cylindrical velocity clustering space.

3.5. *Stability of Clusters and Stars*

We apply the clustering algorithm as well as the 100 random realization process mentioned above to this new high-stability sample. As discussed in Sections 3.3 and 3.4, the high-stability sample comprises only stars identified to be part of some clusters in at least 20 of the 100 random realizations. The clusters found this way are thus more robust than those from the full sample. They are also more stable against merging/splitting due to uncertainties because stars consistently identified as noise have been removed. We now discuss in more detail how we evaluate the stability of the final clusters.

We call the clusters found from the mean values of the clustering parameters the baseline clusters. We use the Jaccard coefficient J (Jaccard 1901) between two clusters from two different realizations to quantify the stability of the cluster. The coefficient J_s^a for a baseline cluster s is defined as the number of common members between the cluster s and a cluster a found in another realization, which we label $N_{s,a}$, divided by the total number of members in the initial cluster s that we label N_s.

$$J_s^a = \frac{N_{s,a}}{N_s}. \tag{1}$$

Baseline clusters s are those from the baseline realization, i.e., clusters found with the mean values, and clusters a are those found in each of the 100 random realizations.[3]

We also define the inverse Jaccard Coefficient $J^\dagger$ as the number of common members divided by the total number of members in a random cluster. More specifically, the $J_s^{a\dagger}$ for a baseline cluster s and a random realization cluster a is therefore defined as

$$J_s^{a\dagger} = \frac{N_{s,a}}{N_a}. \tag{2}$$

To study whether a baseline cluster s is stable, we find its closest cluster in a random realization, i.e., the cluster with which it shares the most members. To do so, we calculate the maximum J_s, that we call $J_s^{r,\max}$, of the baseline cluster s (with respect to all the clusters) in each of the random realization r. We thus record at most 100 values of the $J_s^{r,\max}$ for each baseline cluster s; some baseline clusters are not identified at all in some

of the random realizations, in which cases the $J_s^{r,\max}$ is undefined. We also record the corresponding maximum value of the $J_s^\dagger$ in each realization, called $J_s^{r\dagger,\max}$; this is applying Equation 2 on the same pair of clusters (the baseline s and the random realization r). We note that these $J_s^{r\dagger,\max}$ are therefore not necessarily the maximum possible values for the given random realization and baseline cluster.[4] We examine the $J_s^{r,\max}$ and $J_s^{r\dagger,\max}$ distribution of all the baseline clusters to evaluate their stability.

To distinguish stable from unstable clusters, we first study the distributions of J and $J^\dagger$ of each of the baseline clusters. In Figure 4, we show two examples of the distributions of $J_s^{r,\max}$ and $J_s^{r\dagger,\max}$ for two baseline clusters. To define stability, we take 50% as the cut in $J_s^{r,\max}$ and $J_s^{r\dagger,\max}$ distributions. When over half of the cluster members in the baseline/random cluster are present in the corresponding random/baseline cluster, we say that the baseline cluster is successfully recovered in that random realization, and thus stable. Although the 50% cut is a choice we make, we verified in the Jaccard distributions of all clusters (similarly to those shown in Figure 4) that the stability of the cluster is not sensitive to the exact choice of the cut and is in most cases unambiguous.

More specifically, for a baseline cluster s showing consistently high Jaccard and inverse Jaccard coefficients, specifically $J_s^{r,\max} > 50\%$ and $J_s^{\dagger r,\max} > 50\%$ for all realizations r, the baseline cluster is stable against splitting. Similarly, baseline clusters s with consistently $J_s^{r,\max} < 50\%$ and $J_s^{\dagger r,\max} < 50\%$ are unstable. The more interesting cases are when the J and $J^\dagger$ distributions are inconsistent, as shown in the bottom panel of Figure 4; the high J_s but low $J_s^\dagger$ distributions indicate that the baseline cluster is either absorbing more members, or merging with other clusters in random realizations. We can distinguish the two cases by examining if multiple baseline clusters share the same maximum J cluster in a given random realization. Lastly, we have baseline clusters with the opposite distributions, low J but high $J^\dagger$; these clusters split in random realizations. Applied to the high-stability sample described earlier in this section, we find that most of the Jaccard distributions across the two clustering spaces show consistently high distributions of J and $J^\dagger$.[5] These clusters are identified as the final stable clusters, and the stars within them as core stable stellar members.

---

[3] For illustrative purposes, we compute J_s^a between all baseline clusters and random realization clusters, i.e., for every baseline cluster, we study how much it overlaps with every other cluster in all 100 random realizations. Theoretically, the same thing could be done with any one of the random realizations serving the role of the baseline clusters, because they are ultimately treated as equal. The conclusion about the stability of the cluster membership remains valid, however, regardless of whether we use the baseline clustering as the base, or a random realization as the base. We use the mean values clustering result as the baseline. The only case of clusters that we might miss are the ones that are present in other realizations but not in the baseline.

4. CLUSTERING RESULTS

---

[4] For example, in the case of baseline clusters splitting into multiple smaller clusters in random realizations ($J_s^{r\dagger,\max} \neq J_r^{s,\max}$).

[5] This is not the case if we run HDBSCAN over multiple realizations with the original sample, as a large fraction of the clusters merges and splits, making it difficult to identify the robust groups of stars, and their core member stars.
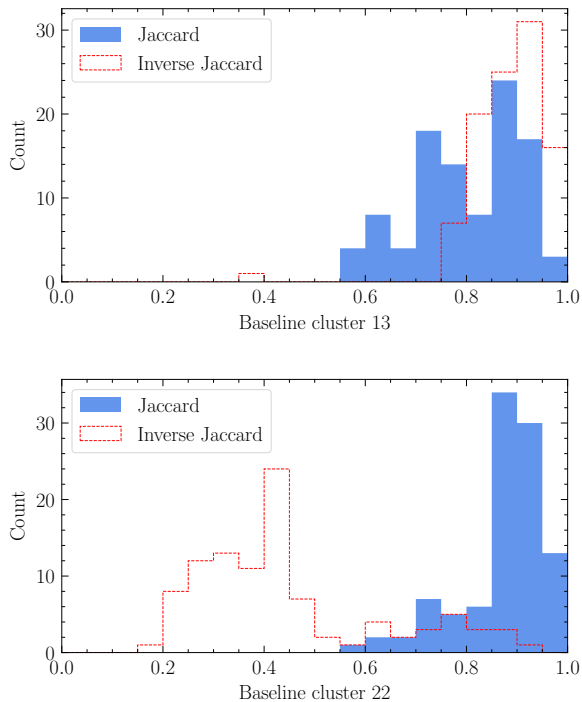
Figure 4. Example Jaccard and inverse Jaccard distributions from clustering results in cylindrical velocity space with Z_{max} cut at 2.5 kpc and N_{stack} cut at 20. Cluster 13 represents a typical stable cluster, whereas cluster 22 represents a more ambiguous case where the Jaccard distribution seems stable while the inverse Jaccard is not. See text for detailed discussion of this case.

We perform HDBSCAN for the high-stability sample (defined in Section 3.5) to obtain the clusters from the stable stars. We repeat the process for both clustering spaces (see Section 3.2). Note that the high-stability samples are different in each of the clustering spaces (and depend on the $N_{\mathrm{stack}}^{\mathrm{cut}}$, which we set to 20 as explained in Section 3.4). All clustering summary results shown here are from a single realization with the mean kinematic parameters of the stars. As discussed in Section 3, the clustering procedure is repeated for 100 random realizations, and all clusters are examined for their stability (see Section 3.5). The reported stable clusters in Tables 1 and 2 are summarized based on the Jaccard stability studies. Therefore, the clusters from the summary figures may not all be classified as stable in the tables. We find 1405 stars in 23 stable clusters in velocity space, and 497 stars in 6 stable clusters in energy and action space.

4.1. *Velocity clusters*

Running the above clustering procedure in velocity space, we show the clustering results in Figure 5. The stars are color-coded by the clusters with which they are associated. We note that even with this high-stability sample clustering space, not all stars are classified to be in one of the final clusters. The final stable clusters from 100 random realizations of HDBSCAN are listed in Table 1.
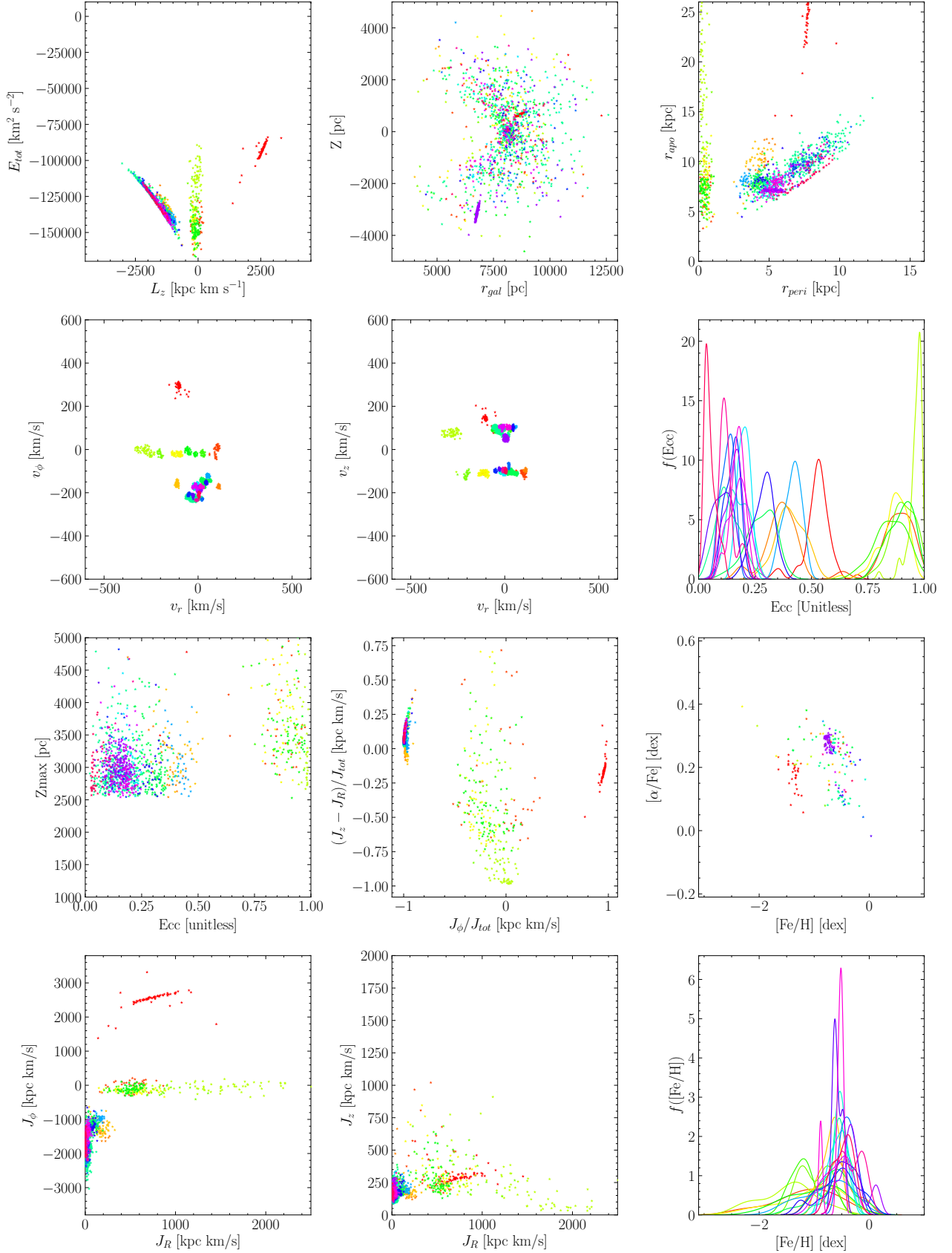
Figure 5. Summary plot for clusters that `HDBSCAN` identified from the high-stability ($N_{\mathrm{stack}} > 20$) sample with Z_{max} $2\,\sigma$ above 2.5 kpc from the cylindrical velocity space.

We see prograde structures with velocity distributions similar to that of the thin and thick disk. One noticeable difference is the slight bias towards positive radial velocity, i.e., more of the identified disk-like prograde clusters are found to be moving away from the galactic center. We discuss each stable cluster identified here in more details in Section 5.

4.2. *Integrals of Motion Clusters*

The clustering results in the Integrals of Motion (Energy and Action) space applied to the high-stability sample are shown in Figure 6. As expected, the clustering results are not the same as those identified in the cylindrical velocity space, as seen in Figure 5. We examine and summarize the properties and stabilities of these clusters in Table 2.

Table 1. Results from sample with N_{stack} greater than 20 in the cylindrical velocity clustering space

Cluster ID	Color	v_R	σ_{v_R}	v_ϕ	σ_{v_ϕ}	v_z	σ_{v_z}	ecc	$[Fe/H]$	$N_{[Fe/H]}$	N_{star}	Stability
		km s^{-1}	km s^{-1}	km s^{-1}	km s^{-1}	km s^{-1}	km s^{-1}		dex			
0	■	-100.93	14.21	291.85	15.01	145.05	16.55	0.53		0	63	Stable
1	■	97.72	11.55	-2.75	19.65	-112.26	10.35	0.88	-1.16	9	39	Stable
2	■	110.0	4.39	-171.9	5.72	-95.88	4.74	0.36	-0.61	7	26	Stable
3	■	-111.46	5.48	-159.53	10.44	-106.72	5.86	0.41	-0.7	11	42	Stable
4	■	-109.77	16.78	-21.44	7.12	-110.45	9.18	0.86	-1.07	16	59	Stable
5	■	-281.08	26.82	-5.67	13.93	72.8	25.23	0.96	-1.47	8	64	Stable
6	■	-204.84	12.42	-19.4	11.72	-117.92	13.3	0.91	-0.99	2	24	Stable
7	■	24.75	8.75	-19.96	9.28	93.65	7.35	0.85	-1.11	4	26	Stable
8	■	-41.78	19.17	-11.6	11.1	97.05	8.69	0.89	-0.99	15	56	Stable
9	■	36.39	14.65	-151.04	11.71	-106.22	6.46	0.28	-0.65	26	167	Stable
10	■	-24.14	23.2	-225.72	8.45	88.6	15.14	0.13	-0.54	49	251	Unstable
11	■	-21.08	3.87	-171.0	8.7	-102.21	5.74	0.18	-0.55	11	54	Stable
12	■	-2.5	3.59	-160.82	5.33	-111.6	4.52	0.2	-0.56	10	37	Stable
13	■	52.34	5.4	-121.0	5.82	104.6	3.98	0.42	-0.78	8	34	Stable
14	■	21.54	2.52	-230.59	2.77	-75.43	10.34	0.13	-0.38	5	28	Unstable
15	■	-49.2	4.82	-207.99	5.06	-99.18	5.09	0.15	-0.54	5	26	Unstable
16	■	43.19	3.43	-153.73	5.16	100.18	7.57	0.29	-0.55	9	32	Stable
17	■	-27.67	3.01	-214.13	6.3	-90.66	4.52	0.1	-0.58	3	24	Unstable
18	■	5.53	6.88	-183.34	7.56	51.14	7.83	0.15	-0.3	6	184	Stable
19	■	-15.19	8.52	-172.05	8.28	103.42	7.02	0.17	-0.59	16	63	Stable
20	■	18.78	7.3	-172.49	4.68	104.28	5.6	0.17	-0.59	5	39	Ambiguous
21	■	-7.8	4.65	-233.56	2.34	-94.81	6.03	0.13	-0.31	2	20	Unstable
22	■	4.87	3.06	-208.89	8.21	-98.67	7.19	0.05	-0.48	13	47	Unstable

Table 2. Results from sample with N_{stack} greater than 20 in the energy and action clustering space

Cluster ID	Color	J_R	σ_{J_R}	J_ϕ	σ_{J_ϕ}	J_z	σ_{J_z}	E_{tot}	$\sigma_{E_{tot}}$	ecc	[Fe/H]	$N_{[Fe/H]}$	N_{star}	Stability
		km kpc s⁻¹	km kpc s⁻¹	km kpc s⁻¹	km kpc s⁻¹	km kpc s⁻¹	km kpc s⁻¹	km² s⁻²	km² s⁻²		dex			
0	■	349.28	97.08	-1167.43	178.0	1155.14	99.66	-106802.56	2941.69	0.44	-1.56	12	65	Stable
1	■	1713.61	90.77	-27.99	104.25	69.67	17.76	-109012.71	2403.22	0.98	-1.07	7	55	Stable
2	■	757.92	134.15	2486.99	242.59	286.34	25.2	-93541.68	3778.38	0.54		0	59	Stable
3	■	573.94	47.09	-52.75	82.0	217.45	21.46	-147907.82	2284.24	0.93	-0.89	34	155	Stable
4	■	16.38	6.44	-2033.83	23.38	119.05	5.36	-120579.56	549.61	0.11	-0.45	16	57	Stable
5	■	17.11	9.01	-1760.66	86.17	133.7	7.04	-126802.74	2026.59	0.11	-0.51	58	287	Unstable
6	■	31.23	10.13	-1248.4	25.81	180.78	9.29	-139561.44	641.08	0.18	-0.56	14	131	Unstable
7	■	24.86	10.26	-1422.58	41.28	161.64	4.6	-135038.12	1151.29	0.15	-0.56	19	106	Stable
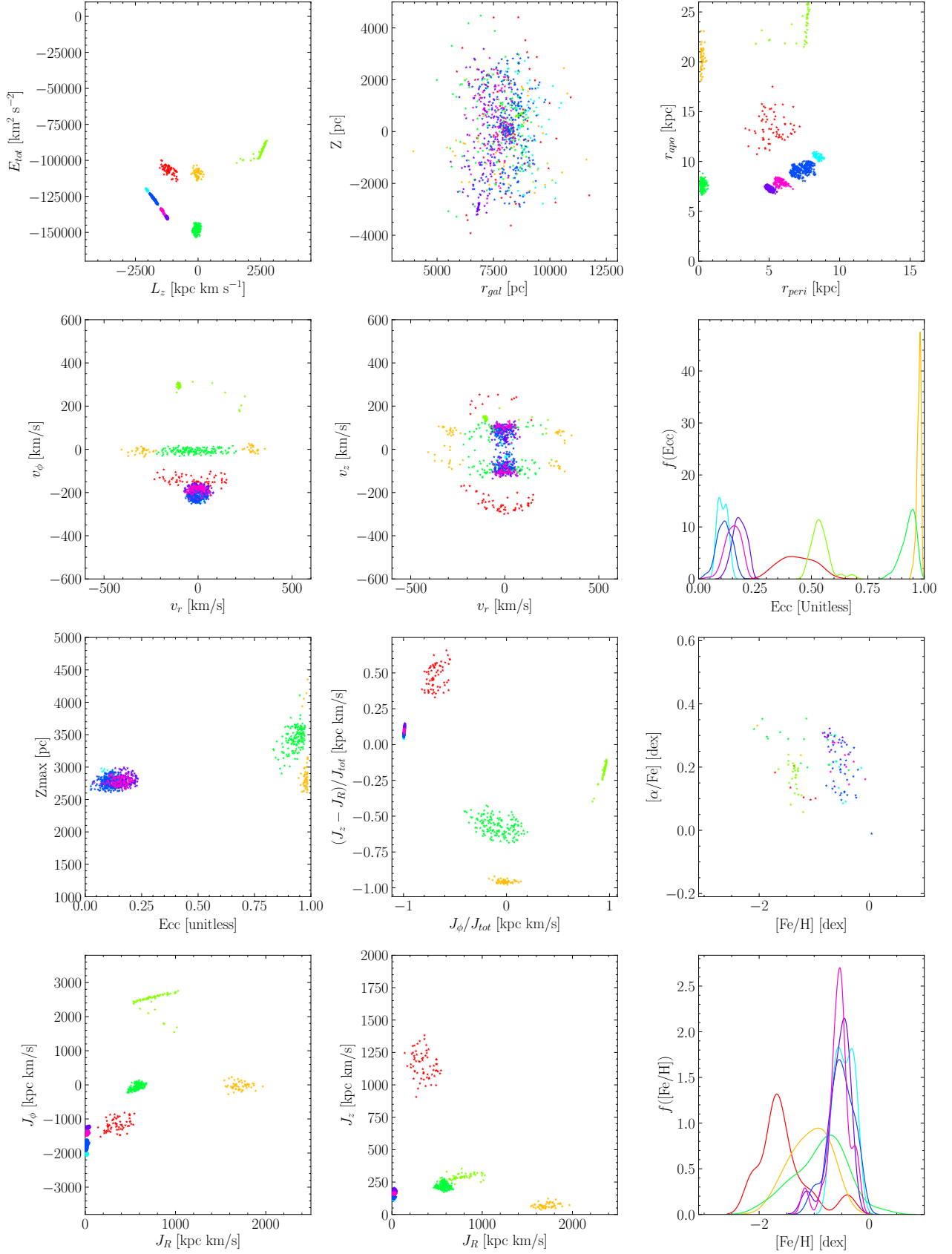
Figure 6. Summary plot for clusters that `HDBSCAN` identified from the high-stability ($N_{\mathrm{stack}} > 20$) sample with $Z_{\max}$ $2\,\sigma$ above 2.5 kpc from the integral of motion space.
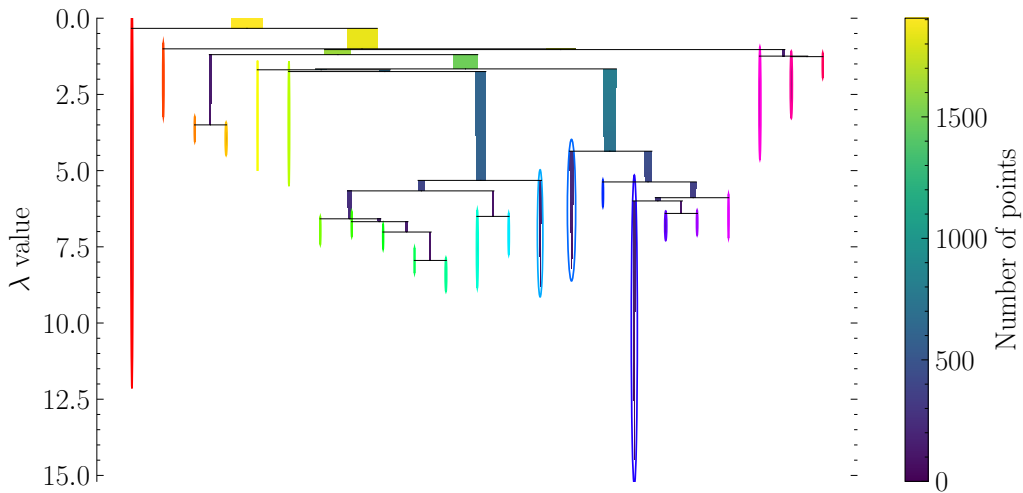
Figure 7. Condensed merger tree for the stacked subsample with $N_{\mathrm{stack}} > 20$ and $Z_{\max}$ $2\,\sigma$ above 2.5 kpc from the cylindrical velocity space. The vertical axis is λ, a measure of distance that HDBSCAN uses to define the edges of the cluster. See McInnes et al. (2017) for more details.

4.3. *Relationship between clusters*

We examine the HDBSCAN merger trees from the clustering results mentioned in Sections 4.1 and 4.2. The trees are extracted by the condensed_tree_ method from the HDBSCAN package. The merger tree allows us to directly see how clusters are related to each other along the hierarchical tree. This is especially important for our clustering method, leaf, which captures the smallest clusters in the sample and is thus designed to subdivide clusters that may be related to each other. It also provides intuition on which axis HDBSCAN primarily uses to distinguish clusters during the clustering process. Figure 7 shows the merger tree for the clustering in velocity space. Identified clusters are shown with a color matching that given in Figure 5. By examining the Figure, we find, for example, that Cluster 0 from Table 1 is the first to be separated from the rest of the clusters, which is sensible given that Cluster 0 is the only retrograde structure found, and it is surrounded by low density points that HDBSCAN deems to be noise. The stars are generally first separated by v_ϕ, where we see a clear division between clusters with and without prograde kinematics.

To study whether multiple clusters belong to the same object, we perform a KS test (Kolmogorov 1933; Smirnov 1948) on the available metallicity of each cluster, which is obtained through cross-matching from LAMOST DR6 (Cui et al. 2012; Zhao et al. 2012).[6] Note that while we classified the clusters' stabilities based on their J and $J^\dagger$ distributions, all clusters from the baseline realization, stable and unstable, are included in the following analysis to avoid inconsistencies caused by removing nodes in the merger tree. Some of the instability may be reflected during the merging process, so it is useful to keep them while inspecting the final results. We note that due to the lack of metallicity measurements for part of the sample, some of the smaller clusters contain too few valid metallicity measurements to provide enough statistics to perform a KS test. In cases where there are fewer than five available [Fe/H] measurements in a given cluster, we skip the comparison, move on to the parent node, and assume the child node can be merged.

We work from the bottom up to compare the metallicities of the clusters on each of the branches. If they are statistically consistent with being drawn from the same group, we merge them together. If not, we keep them as separate groups. We use the KS_2samp routine from the Scipy package (Jones et al. 2001) to perform the KS test. The results are discussed further in Section 5.

---

[6] We note that we use the metallicity measurements from LAMOST DR6 for better statistics in the comparison, as they provide more metallicities than APOGEE DR17, which were featured in the summary plots.
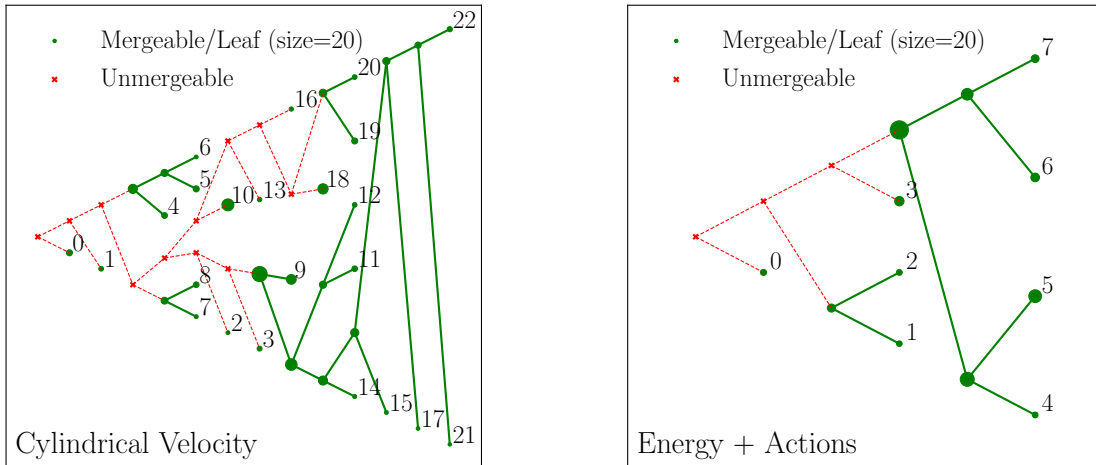
Figure 8. Semi-tree diagrams showing the nodes for the stacked stable subsample with Z_{max} $2\,\sigma$ above 2.5 kpc from the cylindrical velocity space (left) and the energy and action space (right). Size of the nodes is proportional to the size of cluster after merging children nodes. Green in general means the clusters can be merged together either because one or both of the children nodes have less than 10 member or because the they passed the metallicity KS test. Red means the node could not be merged either because the test mentioned above failed or one of the children nodes failed to merge.

5. DISCUSSION AND INTERPRETATION

We compare our final clustering results in the two clustering spaces (see Section 3.2), with parameters set at $Z_{max} > 2.5$ kpc, and $N_{stack} > 20$, against known Milky Way substructures from the literature.

5.1. *Merged clusters*

From Figure 8 (left panel) and Tables 1 and 3, we see that the unstable clusters 14, 15, 17, 21, and 22 are all mergeable (along with the stable clusters 9, 11, and 12). This indicates that the instability of these five clusters against splitting and merging is consistent with the fact that they are compatible with being part of a larger cluster in metallicity space. They are likely all coming from the same larger cluster in velocity space, but only split/merge due to their locations in phase space and the associated uncertainties. Thus, these unstable clusters are fragments of a larger cluster, split in different ways. The member stars in these clusters still remain robust, albeit for a larger cluster.

On the other hand, the unstable cluster 10 has no potentially merging clusters in metallicity space, suggesting that cluster 10 by itself is unlikely a robust cluster and dissolves in velocity space when considering uncertainties. Stellar members in this cluster are thus not robust cluster members.

In addition to the previously identified unstable clusters, we also get stable clusters merged, which is the case for clusters 4-9, 11, 12, 19, and 20 from Table 1. Their corresponding parents, after merging, provide hints for the reason. For example, the newly merged clusters VI and X are likely both part of the thick disk, given the prograde rotational velocity of v_ϕ at ~ -180 km s^{-1}. The `leaf` method we used for `HDBSCAN` divided them into smaller subgroups but their metallicities distributions allow us to confidently say that they can be merged back into a larger group.

We repeat the same process with the clustering result for the integrals of motion space and include the results in Figure 8 (right panel) and Table 4. Clusters 5 and 6, which were previously identified as unstable in Table 2, are merged together with clusters 4 and 7. These results are shown in Figures 9 and 10 for the velocity and integral of motion spaces, respectively. We discuss in the following subsections how the clusters compare with structures known from previous studies. When applicable, we use references from the literature where the kinematic values are obtained and derived similarly to our study to avoid systematic differences, i.e., original data from *Gaia* and similar galaxy potentials used in orbital integrations.

Table 3. Clusters merged based on metallicity distribution from Tab 1.

Cluster ID	Color	v_R	σ_{v_R}	v_ϕ	σ_{v_ϕ}	v_z	σ_{v_z}	ecc	$[Fe/H]$	$N_{[Fe/H]}$	N_{star}	Merged
		km s⁻¹	km s⁻¹	km s⁻¹	km s⁻¹	km s⁻¹	km s⁻¹		dex			
I	■	-100.93	14.21	291.85	15.01	145.05	16.55	0.53	. . .	0	63	[0]
II	■	97.72	11.55	-2.75	19.65	-112.26	10.35	0.88	-1.16	9	39	[1]
III	■	-20.69	35.12	-14.25	11.25	95.97	8.44	0.88	-1.02	19	82	[7 8]
IV	■	110.0	4.39	-171.9	5.72	-95.88	4.74	0.36	-0.61	7	26	[2]
V	■	-111.46	5.48	-159.53	10.44	-106.72	5.86	0.41	-0.7	11	42	[3]
VI	■	8.88	29.44	-178.41	31.77	-101.21	10.86	0.19	-0.56	75	403	[9 11 12 14 15 17 21 22]
VII	■	-24.14	23.2	-225.72	8.45	88.6	15.14	0.13	-0.54	49	251	[10]
VIII	■	52.34	5.4	-121.0	5.82	104.6	3.98	0.42	-0.78	8	34	[13]
IX	■	5.53	6.88	-183.34	7.56	51.14	7.83	0.15	-0.3	6	184	[18]
X	■	-2.2	18.38	-172.21	7.13	103.75	6.53	0.17	-0.59	21	102	[19 20]
XI	■	43.19	3.43	-153.73	5.16	100.18	7.57	0.29	-0.55	9	32	[16]
XII	■	-199.88	81.15	-14.24	13.58	-31.89	93.79	0.91	-1.19	26	147	[4 5 6]

Table 4. Clusters merged based on metallicity distribution from Tab 2.

Cluster ID	Color	J_R	σ_{J_R}	J_ϕ	σ_{J_ϕ}	J_z	σ_{J_z}	E_{tot}	$\sigma_{E_{tot}}$	ecc	[Fe/H]	$N_{[Fe/H]}$	N_{star}	Merged
		km kpc s^{-1}	km kpc s^{-1}	km kpc s^{-1}	km kpc s^{-1}	km kpc s^{-1}	km kpc s^{-1}	km^2 s^{-2}	km^2 s^{-2}		dex			
I	■	349.28	97.08	-1167.43	178.0	1155.14	99.66	-106802.56	2941.69	0.44	-1.56	12	65	[0]
II	■	1219.0	491.27	1273.62	1270.84	181.81	110.47	-101005.77	8362.99	0.75	-1.07	7	114	[1 2]
III	■	573.94	47.09	-52.75	82.0	217.45	21.46	-147907.82	2284.24	0.93	-0.89	34	155	[3]
IV	■	21.64	11.04	-1610.28	262.5	147.97	22.59	-130571.45	6408.31	0.14	-0.52	107	581	[4 5 6 7]
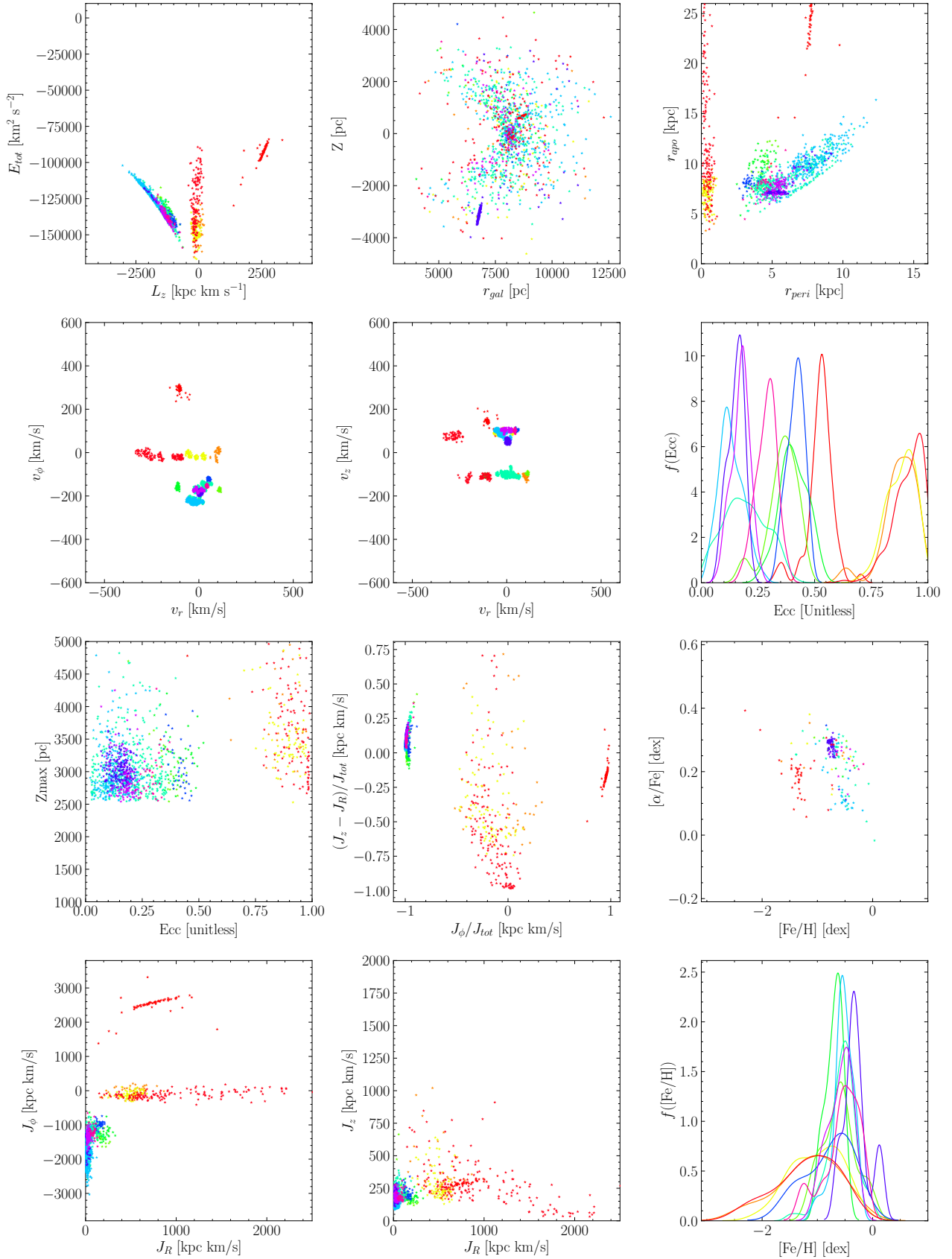
Figure 9. Summary plot for merged clusters that `HDBSCAN` identified in the high-stability ($N_{\mathrm{stack}} > 20$) sample with $Z_{\max}$ $2\,\sigma$ above 2.5 kpc from the cylindrical velocity space. Note the colors do not match those from Figure 5, but those quoted in Table 3.
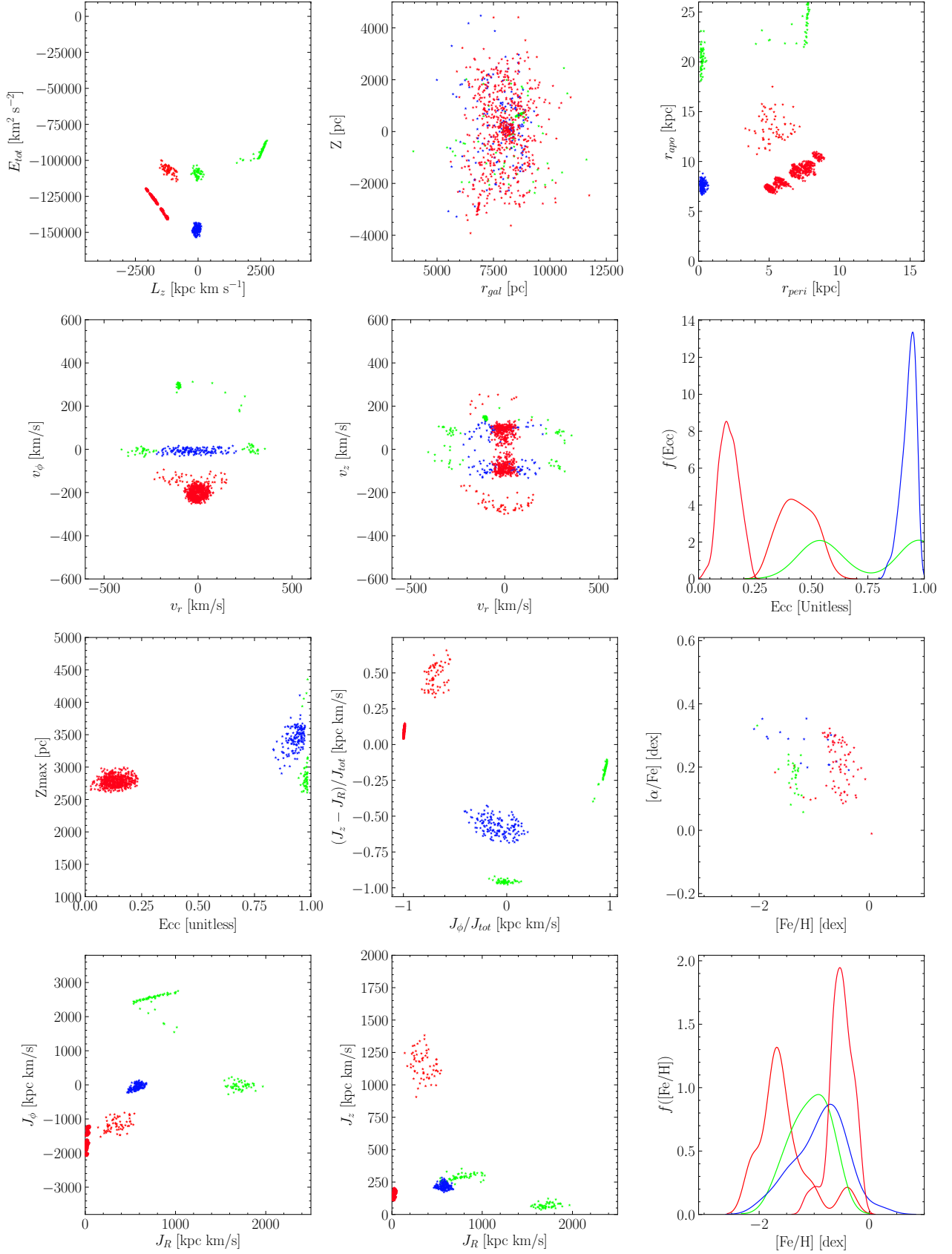
Figure 10. Summary plot for merged clusters that `HDBSCAN` identified in the high-stability ($N_{stack} > 20$) sample with Z_{max} 2σ above 2.5 kpc from the energy and action space. Note the colors do not match those from Figure 6

5.2. *Velocity space*

In this section, we associate clusters found in the velocity clustering space with known structures in the literature by discussing their mean kinematics and chemical characteristics in turn. A summary of the all the clusters discussed here can be found in Figure 9, and Table 3.

We start with the two globular clusters identified, NGC 3201 (cluster I shown as dark red in Figure 9) and NGC 104 (cluster IX, shown as dark blue in Figure 9). We find these clusters at $(l, b) = (277.21, 8.63)$ degrees and $(305.88, -44.90)$ degrees, and heliocentric distances of 4.22 kpc and 4.33 kpc, respectively. These coordinates are consistent with the values of $(l, b) = (277.23, 8.64)$ degrees and $(305.89, -44.90)$ degrees from Harris (1996, 2010) considering the half-light radius of these two clusters are at 3.1 arcmin and 3.17 arcmin, respectively. The heliocentric distances in Harris (1996, 2010) are 4.9 and 4.5 kpc for NGC 3201 and NGC 104, respectively, where we attribute the disagreement with our values to systematic uncertainties in the different methods used in measuring distances, i.e., photometry vs. astrometry. Finding these globular clusters within our framework is a validation of our clustering method. It is, however, worth noting that these two globular clusters appear more extended along the line of sight than they actually are from dedicated globular cluster studies (see Harris 2010, and references therein). This is a common effect in galactic coordinate transformation caused by the uncertainties in the distance to the sources. First, this further emphasizes the importance of incorporating uncertainties into the clustering. Additionally, a similar effect would be present for the entire sample and as a result systematically increase the scale height of the thin disk at high galactic latitude. This plays a role in interpreting the prograde structures we identify, which we discuss below.

Our newly identified clusters II, III, XII have almost no rotational motion and low metallicity. Their chemical characteristics are overall consistent with being part of GSE, with mean [Fe/H] = -1.16, -1.02, and -1.19, respectively. These values agree with literature estimates of the metallicity of the GSE, which ranges from [Fe/H] ~ -1.6 to -1.1, depending on the selection criterion (Helmi et al. 2018; Necib et al. 2019a; Naidu et al. 2020). Because of the $Z_{\max}$ cut we applied, the stars identified as part of these clusters most likely correspond to the high vertical motion portion of the GSE. The majority of the GSE would be left out in the initial cut, yet the fact that the overdensity is still identified suggests the GSE has a non-negligible tail in high vertical velocity distribution. Clusters II and XII (shown in orange and red in Figure 9) have the known high radial velocities of the GSE (Belokurov et al. 2018; Helmi et al. 2018). However, Cluster III (shown in yellow) does not. It could be that this cluster, which has eccentricities and

metallicities consistent with clusters II and XII, encompasses the stars that connect the positive and negative radial velocity lobes of the GSE.

We now discuss the possibility of our prograde clusters being the high J_z tail of the thin disk or thick disk. Knowing that the uncertainties in the distances can systematically increase the scale height of the disk, stars originally on the exponential tail of the disk height distribution could be pushed outward into our selection region, $Z_{\max}$ greater than 2.5 kpc, as was shown earlier in Figure 2. We thus expect there to be a significant amount of disk stars in the final high-stability sample. Cluster VII (in cyan), despite the significant vertical motion, does otherwise appear to be part of the thin disk. The cluster has rotational velocity $v_\phi = -225.72$ km s^{-1} and eccentricity of 0.13, consistent with being part of the thin disk. The mean metallicity of -0.54 and low α-abundance also support the thin disk origin.

Additionally, clusters IV, V, VI, X, colored as fluorescent green, green, turquoise, and purple, respectively, sit in between the two groups mentioned above, with kinematics more consistent with that of the thick disk, and average v_ϕ approximately 150 to 180 km s^{-1}. The current estimate of the canonical thick disk scale height from recent literature study is 0.9 ± 0.2 kpc (see Bland-Hawthorn & Gerhard (2016) for a review on galactic disc parameters). The metallicity distributions of these clusters peak between -1 and 0 dex, with overall high α-abundances, which are consistent with these stars being part of the canonical thick disk. We thus associate them as part of the thick disk. Clusters VIII (in dark blue) and XI (in pink), while being prograde, appear distinct from the thin disk with metallicity distributions extending lower than -1. This can be taken as a sign of these clusters containing accreted stellar populations or a portion of the metal-weak Atari disk (Norris et al. 1985; Morrison 1990; Chiba & Beers 2000; Mardini et al. 2022).

5.3. *Integrals of Motion Space*

Similarly to the above, we associate the following clusters identified in energy and action space with known Milky Way substructures. We find four clusters that we list in Table 4, and show in Figure 10. Cluster I, shown in the Figure colored in dark red, closely resembles the Helmi stream (Helmi et al. 1999), which is expected due to its well-known large vertical motion. Thus most of its members pass the $Z_{\max}$ cut. The mean kinematics and metallicity of the cluster identified in our study are $J_\phi = -1.17^{\pm 0.10} \times 10^3$ kpc km s^{-1}, $E_{tot} = -10.68^{\pm 0.29} \times 10^4$ km^2 s^{-2}, and [Fe/H] = -1.56. They agree with literature selection of the Helmi stream in L_z in $[-1.7, -0.75] \times 10^3$ kpc km s^{-1} (Koppelman et al. 2019b), $E_{tot} = -10.3 \times 10^4$ km^2 s^{-2}, and peak [Fe/H] ranging from -1.5 to -1.3 (Naidu et al. 2020). As the merger event associated with these streams happened approximately 5-8 Gyr ago (Koppelman et al. 2019b),

the stream does not show a significant coherent spatial structure. Its stars distribute spatially similar to the background stars, except being confined by Galactic radial distance (Koppelman et al. 2019b).

Cluster II, shown in green, is a mix of three substructures. Merging based on metallicity alone has caused structures that are obviously not from the same group to be merged. Thus, instead of discussing the merged cluster II, we discuss pre-merging clusters 1 and 2, together with cluster III, i.e., cluster 3.

The radial motion dominated clusters (pre-merging clusters 1 and 3), resembling the GSE, are identified with much fewer clusters than in velocity space, and they are mainly distinguished by energy rather than radial velocity. Both clusters have mean metallicity [Fe/H] ~ -1, roughly consistent with literature values, but the lower energy cluster 3 shows potential for contamination from the high metallicity in-situ halo at [Fe/H] ~ -0.5 and the big splash (stars formed in protodisc and have orbit altered to the highly eccentric orbit by the last major merger event) with metallicity > -0.7 from Belokurov et al. (2020). The higher energy cluster, on the other hand, appears to be more in line with the metal-poor nature of an accreted structure like the GSE.

Globular cluster NGC 3201 (our pre-merging cluster 2) is identified as in the cylindrical velocity space. There are, however, a few additional members identified in this cluster, which are most likely not true members of the globular cluster. We suspect they actually belong to the high energy retrograde structure Sequoia Myeong et al. (2019), and are instead mis-classified to be part of this globular cluster due to our HDBSCAN parameter setting. Namely, the minimum cluster size of 20 prohibited these Sequoia stars from forming their own cluster. Repeating HDBSCAN clustering in the full sample space with minimum cluster size reduced to 10, the result indicates Sequoia-like stars are identified separately as their own cluster. We are thus confident that we may safely remove the globular cluster core members and treat the rest of the cluster as a significant overdensity. We can do so given the globular cluster's well-known coordinates ($(l, b) = (277.21, 8.63)$ degrees) and angular radius ($0.05°$) (Harris 2010) in the sky (see the details of this overdensity in Figure S6). Note that the few stars that are left have no metallicities available.

There has been a discussion in the literature about the existence of multiple populations within the currently identified retrograde structure named Sequoia, i.e., Arjuna and I'itoi. The three structures are discussed in more detail in Naidu et al. (2020). The latter two are discovered in chemical space as separate peaks, with [Fe/H] of $-1.6, -1.2, < -2$ for Sequoia, Arjuna, and I'itoi, respectively. The lack of metallicity measurements for our cluster prevents us from resolving potential population compositions of this prograde structure. Like GSE, Sequoia is also believed to have most of its stars having a zero mean v_z. Thus, our initial

cut has preferentially removed Sequoia. Despite that, HDBSCAN identifies an overdensity at high Z_{max}, signaling that Sequoia may be more kinematically heated and vertically extended than previously thought.

We associate multiple prograde structures (all in merged cluster IV, shown in dark red) with the thin and the thick disk, as they have rotational velocity of ~ -200 km s^{-1} and metallicity ~ -0.5 dex, consistent with the disk of the Milky Way (Bland-Hawthorn & Gerhard 2016). The position of these clusters in the Z_{max} vs. eccentricity plane also suggest the possibility of these stars being the high vertical motion end of the velocity distribution of the thin disk and thick disk. We evaluated whether these stars belong to Nyx; crossmatching Nyx and Nyx-2 with the high-stability sample in integrals of motion space yields no match. In fact, the majority of the Nyx stars are cut out by our Z_{max} cut, so we would not expect this cluster to be associated with the Nyx.

5.4. Comparison with Other Works

Previous work has been done in identifying local substructures self-consistently with only kinematic data as input. We now compare the results of our clustering algorithm to those of previous studies.

We first discuss the work of Sofie Lövdal et al. (2022); Ruiz-Lara et al. (2022), which shares similar scientific goals and approaches as this study. Sofie Lövdal et al. (2022) adopted a *Gaia* eDR3 sample with crossmatched radial velocities from other spectroscopic surveys than APOGEE and LAMOST. The halo sample, used for clustering, is isolated by applying a v_{LSR} cut. They opted for the single linkage tree as the clustering algorithm, combined with Mahalanobis distances (Mahalanobis 1936) for final cluster and membership selections. While different, HDBSCAN is inherently also a linkage tree algorithm. The clustering space of Sofie Lövdal et al. (2022) is limited to energy and angular momenta, and uncertainties in these quantities have not been taken into account.

While both Sofie Lövdal et al. (2022) and our study identified structures such as the GSE, Helmi Stream, and Sequoia, we do not identify some of the structures (e.g., Thamnos) identified in Sofie Lövdal et al. (2022) mostly because of the different cuts applied. The Z_{max} cut has removed the majority of the structures to the point that HDBSCAN can no longer pick up any overdensities in phase space. This is likely the case for Thamnos, which is known to be associated with a low stellar mass accretion event that happened a long time ago, a low metallicity, and low total energy. The mean $\langle v_z \rangle$ for Thamnos is consistent with being zero from previous studies, and its current identified member count is lower than that of GSE or Sequoia. Moreover, our average cluster size is significantly smaller due to the different approach we used for selecting robust cluster members with uncertainties considered, along with the

different algorithm used. While some clusters identified in their study also appear in similar phase space locations in single realizations of this study, the majority of the stars within these overdensities, as discussed in Section 3.3, do not robustly belong to said clusters when all random realizations are taken into account. We see in Figure S1 that most of the stars ever associated with any cluster by HDBSCAN in the 100 random realizations have N_{stack} less than 10, i.e., they are flagged as noise 90% of the time. The robust clusters and their constituents are thus a smaller subset of what one would get by applying HDBSCAN to only the full sample with nominal value inputs.

Ruiz-Lara et al. (2022) used a crossmatched chemical information and mass-age relation to characterize the identified clusters in Sofie Lövdal et al. (2022). The membership selection was validated with isochrone fitting and metallicity distribution function study, where there are available matches in spectroscopic surveys. We do not carry out a similar validation because requiring stability of the clusters comes at the expense of statistics. As such, we cannot reliably characterize the progenitors with such few available chemical abundances. While our sample size does allow further study of the structure's color-magnitude diagram and potential comparison with synthetic color-magnitude diagrams, factoring in the observational uncertainties from the data and theoretical uncertainties from the stellar evolution models is not a trivial effort (Cignoni & Tosi 2010). We thus defer characterizing our robust clusters with synthetic color-magnitude diagram fitting procedures to a future study.

We also compare our results with those from Naidu et al. (2020), where selections are more based on physical intuition. Again, we recover the GSE, Helmi Stream, and Sequoia, but miss Thamnos for the same reasons mentioned above. We also do not detect any structure that resembles Aleph or Wukong, both reported to have high J_z(Naidu et al. 2020). While Aleph has a relatively high vertical motion, its selection required chemical information which is not available to our study. Wukong is a structure found to be two overdensities near the margin of the GSE in the E_{tot} vs. L_z plane. With only kinematic information, we suspect that incorporating uncertainties has caused the cluster to become unstable and thus make it more difficult for HDBSCAN to robustly separate it from the GSE and background. We also point out that Naidu et al. (2020) focused on stars 3 kpc away from the solar neighborhood, so it is also likely that these two structures are only present/or dominate at high galactic latitude, and thus we do not have large enough statistics within our sample to identify such kinds of structures.

Our clustering results give two clusters associated with the GSE. Donlon et al. (2022) discussed the GSE being composed of multiple components, namely the VRM, Nereus, and Cronus, using kinematics and metallicities for *Gaia* eDR3 dwarf stars. We compare our pre-

merging clusters 1 and 3 in the integrals of motion space with the three radial merger events identified by Donlon et al. (2022). Our pre-merging cluster 1 resembles the VRM and Nereus with its high energy and double-lobed v_r velocity profile, but the average metallicity of our cluster [Fe/H] ~ -1.07 is higher than those of the VRM and Nereus at -1.7 and -2.1 respectively. Similarly, the lower energy cluster 3 has slightly higher metallicity [Fe/H] ~ -0.89 than the Cronus at -1.2. Further, while the Cronus was shown to be prograde with $L_z \sim -400$ kpc km s^{-1}, our low energy GSE-like cluster is consistent with being non-rotating. In short, while our clustering results in the integral of motion space separate the GSE into high-energy and low-energy components, the metallicities do not show as significant a difference as that shown in Donlon et al. (2022). The discrepancy may be a combined result of systematic differences in metallicity derivation, given that Donlon et al. (2022) used photometric metallicity estimates calibrated using a collection of spectroscopic survey catalogs in the literature (see Section 2.3 in Kim & Lépine (2022)) while we only used LAMOST DR6, and/or potential contamination from in-situ stars in our clusters given that our clustering is based solely on kinematic properties. For a similar reason, we are not able to distinguish potential constituents in our high eccentricity clusters the same way as in Myeong et al. (2022), where chemical abundances from APOGEE DR17 (Abdurro'uf et al. 2022) and GALAH DR3 (Buder et al. 2021) are used to construct the chemo-dynamical space for Gaussian Mixture Modeling.

6. INTERPRETATION AND CONCLUSIONS

In this section, we discuss both the challenges in identifying local structures using clustering algorithms as well the potential that new approaches can deliver with current and future data with regards to the detailed exploration of the Galaxy's assembly and accretion history.

In general, while satellite galaxies that have merged or are in the process of merging with the Milky Way can principally be extracted with clustering tools, the observed signal is often too weak compared to the background (e.g. structures within the disk) and identification becomes even more challenging with increasing measurement uncertainties. Accordingly, the current standard practice of largely mitigating unreliable selections has been focused on using either chemical abundance information or isochrone fitting techniques to validate the stellar membership. However, this approach, when applied to the entirety of the Galaxy, will be limiting going forward; chemical information is severely restricted by the difficulty in obtaining medium or high-resolution spectroscopic metallicities and abundances for quantities of stars that are comparable to those of large-scale astrometric and photometric surveys such as *Gaia*. Isochrone fitting of a collection of stars is dependent on the completeness and selection function of

any sample. These methods of a posteriori resorting the data also partially undermine the purpose of using an unsupervised machine learning algorithm to handle large data sets and make objective decisions unaffected by human biases.

Another problem on its own is measurement uncertainties associated with input kinematic data. Unfortunately, the current scope of our study is severely limited by detailed and precise 6D kinematics information, especially for fainter stars that probe deep into the galactic halo, when measurement uncertainties become larger or no information is available at all. Membership assignments by hierarchical clustering algorithms such as HDBSCAN are generally unreliable when uncertainties are not taken into account. For example, when considering stars that are associated with a random cluster in more than one out of 100 random clustering realizations, the majority of the stars are often assigned to be noise in the other 99 realizations. However, this is not too surprising. Hierarchical clustering algorithms, e.g., single-linkage algorithms such as HDBSCAN, rely on first building some form of a hierarchical merger tree, which can alter significantly when data points are shifted within their respective uncertainties. A changed tree will naturally lead to altered findings and as such will yield unreliable results when it comes to identifying new overdensities and their constituents. Thus, the results from applying such algorithms straight to the nominal mean values of the input parameters cannot be trusted. *We thus stress the need for numerical techniques that produce the most reliable and reproducible clustering results, by taking advantage of incorporating existing observational and astrometric uncertainties in the clustering algorithms. Specifically, we propose a more robust method of utilizing HDBSCAN in identifying local stable stellar overdensities in kinematic space.*

To overcome these challenges and to identify robust and reliable clusters, in this study, we use *Gaia* eDR3 astrometry data together with line-of-sight radial velocity from *Gaia* DR2 to identify clusters in the solar neighborhood using HDBSCAN. In our novel procedure, we successfully incorporate measurement uncertainties in the clustering algorithm to produce stable and robust clusters and recover previously known structures in the Milky Way, specifically the GSE, Sequoia, the Helmi Stream, and the globular clusters NGC 3201 and NGC 104. We achieved this by resampling the input data, repeating the clustering process, and treating each random realization equally. We then incorporate measurement uncertainties in the clustering algorithm by resampling the input data, repeating the clustering process, and treating each random realization equally. This technique allows us to confidently isolate the most stable and robust cluster members by stacking the clustering results from each realization and removing those that are associated with noise in more than 20 (out of 100) re-

alizations. These cluster members are then re-clustered into our final set of stable clusters.

When properly incorporating measurement uncertainties in a routine fashion, the resulting robust cluster members will naturally be much fewer than those that would be obtained from applying algorithms to only the nominal values. We have thus focused in this study on retrieving stellar core members of structures near us. Regardless, these results already provide candidate structures that could be targeted for follow-up observations with future spectroscopic surveys, such as 4MOST (de Jong et al. 2019) and WEAVE (Dalton et al. 2012). Since obtaining spectroscopic data requires significant amounts of time, as more clusters as well as cluster candidates are being identified, targeted follow-up will be maximally efficient, ensuring a high discovery rate.

To further increase efficiency and maximal identification of as many cluster member stars as possible, as a next step we anticipate expanding our technique to include a "cluster re-building" component in which we start with the robust clusters and then carry out an additional member selection with progressively loosened stability criteria to eventually re-build the full clusters step-by-step, still with uncertainties factored in. This approach makes use of the fact that the existence of the cluster is no longer in question, and instead focuses efforts on finding the complete stellar membership.

More broadly, our technique of providing precise identifications of substructure signatures has the potential to go beyond finding just accreted structures. In particular, in the galactic disk, studies of moving groups have long revealed many overdensities of stars moving in common orbits (Antoja et al. 2018), with the most dominant ones being the branches of Sirius, Coma Berenices, Hyades-Pleiades, and Hercules. These local overdensities, proposed to be induced by dynamical resonances, past perturbations, and/or non-axisymmetric features of the Milky Way, are all prime targets of research and provide valuable insights into the formation and evolution of the galactic disk (see, e.g., Appendix B of Trick et al. (2019) for a short review). New moving groups are still being discovered thanks to constantly improving methodologies (Ramos et al. 2018; Bernet et al. 2022; Lucchini et al. 2022). Identifying these overdensities in the disk with high confidence requires careful treatment of the uncertainties, as the structures will most likely be accompanied by strong background noise. Lucchini et al. (2022), for example, incorporated various measurement uncertainties with wavelet transforms, which is another promising way to maximize unsupervised data analysis outputs.

These novel data analysis approaches, and as more and deeper data becomes available, from both space missions, such as *Gaia*, and ground missions, such as the Vera Rubin Observatory Legacy Survey of Space and Time (LSST) (Ivezić et al. 2019), showcase the huge discovery potential for stellar (sub)structures in the Milky

Way. We thus anticipate that many more delicate, thus far hidden clusters will be discovered. But success will rest solely on our ability to rely on unsupervised machine learning algorithms, such as HDBSCAN, to provide trustworthy outputs. We can only trust algorithms when we factor in measurement uncertainties that, of course, are always present in observational astronomy.

In closing, understanding in detail how accurate these techniques and algorithms are given the current level of uncertainties in observational measurements is an important step towards building a complete picture of the Milky Way, as well as towards providing improved modeling capabilities of the local DM phase space distribution.

We thus encourage future clustering studies to begin testing and incorporating uncertainties into their new generation of techniques and unsupervised machine learning algorithms, to acquire reliable and robust selections of substructures and their member stars based on kinematic information only.

REFERENCES

Abdurro'uf, Accetta, K., Aerts, C., et al. 2022, ApJS, 259, 35, doi: 10.3847/1538-4365/ac4414

Antoja, T., Helmi, A., Romero-Gómez, M., et al. 2018, Nature, 561, 360, doi: 10.1038/s41586-018-0510-7

Astropy Collaboration, Robitaille, T. P., Tollerud, E. J., et al. 2013, A&A, 558, A33, doi: 10.1051/0004-6361/201322068

Astropy Collaboration, Price-Whelan, A. M., Sipőcz, B. M., et al. 2018, AJ, 156, 123, doi: 10.3847/1538-3881/aabc4f

Behroozi, P., Wechsler, R. H., Hearin, A. P., & Conroy, C. 2019, MNRAS, 488, 3143, doi: 10.1093/mnras/stz1182

Belokurov, V., Erkal, D., Evans, N. W., Koposov, S. E., & Deason, A. J. 2018, MNRAS, 478, 611, doi: 10.1093/mnras/sty982

Belokurov, V., Sanders, J. L., Fattahi, A., et al. 2020, MNRAS, 494, 3880, doi: 10.1093/mnras/staa876

Belokurov, V., Zucker, D. B., Evans, N. W., et al. 2006, ApJL, 642, L137, doi: 10.1086/504797

Bennett, M., & Bovy, J. 2019, MNRAS, 482, 1417, doi: 10.1093/mnras/sty2813

Bernet, M., Ramos, P., Antoja, T., et al. 2022, arXiv e-prints, arXiv:2206.01216. https://arxiv.org/abs/2206.01216

Binney, J., & Spergel, D. 1982, ApJ, 252, 308, doi: 10.1086/159559

Bird, S. A., Xue, X.-X., Liu, C., et al. 2021, ApJ, 919, 66, doi: 10.3847/1538-4357/abfa9e

Bland-Hawthorn, J., & Gerhard, O. 2016, ARA&A, 54, 529, doi: 10.1146/annurev-astro-081915-023441

Bovy, J. 2015, ApJS, 216, 29, doi: 10.1088/0067-0049/216/2/29

Brauer, K., Andales, H. D., Ji, A. P., et al. 2022, arXiv e-prints, arXiv:2206.07057. https://arxiv.org/abs/2206.07057

Buder, S., Sharma, S., Kos, J., et al. 2021, MNRAS, 506, 150, doi: 10.1093/mnras/stab1242

Buder, S., Lind, K., Ness, M. K., et al. 2022, MNRAS, 510, 2407, doi: 10.1093/mnras/stab3504

Bullock, J. S., & Johnston, K. V. 2005, ApJ, 635, 931, doi: 10.1086/497422

Carollo, D., & Chiba, M. 2021, ApJ, 908, 191, doi: 10.3847/1538-4357/abd7a4

Chiba, M., & Beers, T. C. 2000, AJ, 119, 2843, doi: 10.1086/301409

Chiti, A., Frebel, A., Mardini, M. K., et al. 2021, ApJS, 254, 31, doi: 10.3847/1538-4365/abf73d

Cignoni, M., & Tosi, M. 2010, Advances in Astronomy, 2010, 158568, doi: 10.1155/2010/158568

Conroy, C., Bonaca, A., Cargile, P., et al. 2019, ApJ, 883, 107, doi: 10.3847/1538-4357/ab38b8

Cooper, A. P., Cole, S., Frenk, C. S., et al. 2010, MNRAS, 406, 744, doi: 10.1111/j.1365-2966.2010.16740.x

Cui, X.-Q., Zhao, Y.-H., Chu, Y.-Q., et al. 2012, Research in Astronomy and Astrophysics, 12, 1197, doi: 10.1088/1674-4527/12/9/003

Dalton, G., Trager, S. C., Abrams, D. C., et al. 2012, in Society of Photo-Optical Instrumentation Engineers (SPIE) Conference Series, Vol. 8446, Ground-based and Airborne Instrumentation for Astronomy IV, ed. I. S. McLean, S. K. Ramsay, & H. Takami, 84460P, doi: 10.1117/12.925950

de Jong, R. S., Agertz, O., Berbel, A. A., et al. 2019, The Messenger, 175, 3, doi: 10.18727/0722-6691/5117

Donlon, Thomas, I., Newberg, H. J., Kim, B., & Lépine, S. 2022, ApJL, 932, L16, doi: 10.3847/2041-8213/ac7531

Drimmel, R., & Poggio, E. 2018, Research Notes of the American Astronomical Society, 2, 210, doi: 10.3847/2515-5172/aaef8b

Drukier, A. K., Freese, K., & Spergel, D. N. 1986, PhRvD, 33, 3495, doi: 10.1103/PhysRevD.33.3495

Fattahi, A., Deason, A. J., Frenk, C. S., et al. 2020, MNRAS, 497, 4459, doi: 10.1093/mnras/staa2221

Feuillet, D. K., Feltzing, S., Sahlholdt, C., & Bensby, T. 2022, arXiv e-prints, arXiv:2206.03875. https://arxiv.org/abs/2206.03875

Frebel, A., & Norris, J. E. 2015, ARA&A, 53, 631, doi: 10.1146/annurev-astro-082214-122423

Freeman, K., & Bland-Hawthorn, J. 2002, ARA&A, 40, 487, doi: 10.1146/annurev.astro.40.060401.093840

Frenk, C. S., & White, S. D. M. 2012, Annalen der Physik, 524, 507, doi: 10.1002/andp.201200212

Gaia Collaboration, Prusti, T., de Bruijne, J. H. J., et al. 2016, A&A, 595, A1, doi: 10.1051/0004-6361/201629272

Gaia Collaboration, Brown, A. G. A., Vallenari, A., et al. 2018, A&A, 616, A1, doi: 10.1051/0004-6361/201833051

—. 2021, A&A, 649, A1, doi: 10.1051/0004-6361/202039657

Gómez, F. A., Helmi, A., Brown, A. G. A., & Li, Y.-S. 2010, MNRAS, 408, 935, doi: 10.1111/j.1365-2966.2010.17225.x

Goodman, M. W., & Witten, E. 1985, PhRvD, 31, 3059, doi: 10.1103/PhysRevD.31.3059

Gravity Collaboration, Abuter, R., Amorim, A., et al. 2018, A&A, 615, L15, doi: 10.1051/0004-6361/201833718

Griffen, B. F., Ji, A. P., Dooley, G. A., et al. 2016, ApJ, 818, 10, doi: 10.3847/0004-637X/818/1/10

Gudin, D., Shank, D., Beers, T. C., et al. 2021, ApJ, 908, 79, doi: 10.3847/1538-4357/abd7ed

Harris, W. E. 1996, AJ, 112, 1487, doi: 10.1086/118116

—. 2010, arXiv e-prints, arXiv:1012.3224.
https://arxiv.org/abs/1012.3224

Helmi, A. 2020, ARA&A, 58, 205,
doi: 10.1146/annurev-astro-032620-021917

Helmi, A., Babusiaux, C., Koppelman, H. H., et al. 2018,
Nature, 563, 85, doi: 10.1038/s41586-018-0625-x

Helmi, A., Veljanoski, J., Breddels, M. A., Tian, H., &
Sales, L. V. 2017, A&A, 598, A58,
doi: 10.1051/0004-6361/201629990

Helmi, A., & White, S. D. M. 1999, MNRAS, 307, 495,
doi: 10.1046/j.1365-8711.1999.02616.x

Helmi, A., White, S. D. M., de Zeeuw, P. T., & Zhao, H.
1999, Nature, 402, 53, doi: 10.1038/46980

Hernquist, L. 1990, ApJ, 356, 359, doi: 10.1086/168845

Herzog-Arbeitman, J., Lisanti, M., Madau, P., & Necib, L.
2018a, PhRvL, 120, 041102,
doi: 10.1103/PhysRevLett.120.041102

Herzog-Arbeitman, J., Lisanti, M., & Necib, L. 2018b,
JCAP, 2018, 052, doi: 10.1088/1475-7516/2018/04/052

Hopkins, P. F., Wetzel, A., Kereš, D., et al. 2018, MNRAS,
480, 800, doi: 10.1093/mnras/sty1690

Hunter, J. D. 2007, Computing in Science and Engineering,
9, 90, doi: 10.1109/MCSE.2007.55

Ibata, R. A., Gilmore, G., & Irwin, M. J. 1994, Nature,
370, 194, doi: 10.1038/370194a0

Ivezić, Ž., Kahn, S. M., Tyson, J. A., et al. 2019, ApJ, 873,
111, doi: 10.3847/1538-4357/ab042c

Jaccard, P. 1901, Bulletin de la Societe Vaudoise des
Sciences Naturelles, 37, 241, doi: 10.5169/seals-266440

Johnston, K. V. 1998, ApJ, 495, 297, doi: 10.1086/305273

Johnston, K. V., Bullock, J. S., Sharma, S., et al. 2008,
ApJ, 689, 936, doi: 10.1086/592228

Johnston, K. V., Hernquist, L., & Bolte, M. 1996, ApJ,
465, 278, doi: 10.1086/177418

Jones, E., Oliphant, T., Peterson, P., & et al. 2001, SciPy:
Open source scientific tools for Python, online.
http://www.scipy.org/

Jungman, G., Kamionkowski, M., & Griest, K. 1996, PhR,
267, 195, doi: 10.1016/0370-1573(95)00058-5

Jurić, M., Ivezić, Ž., Brooks, A., et al. 2008, ApJ, 673, 864,
doi: 10.1086/523619

Keller, S. C., Schmidt, B. P., Bessell, M. S., et al. 2007,
PASA, 24, 1, doi: 10.1071/AS07001

Kim, B., & Lépine, S. 2022, MNRAS, 510, 4308,
doi: 10.1093/mnras/stab3671

Knebe, A., Gill, S. P. D., Kawata, D., & Gibson, B. K.
2005, MNRAS, 357, L35,
doi: 10.1111/j.1745-3933.2005.08666.x

Kolmogorov, A. N. 1933, G. Ist. Ital. Attuari., 4, 83

Koppelman, H. H., Helmi, A., Massari, D., Price-Whelan,
A. M., & Starkenburg, T. K. 2019a, A&A, 631, L9,
doi: 10.1051/0004-6361/201936738

Koppelman, H. H., Helmi, A., Massari, D., Roelenga, S., &
Bastian, U. 2019b, A&A, 625, A5,
doi: 10.1051/0004-6361/201834769

Lee, Y. S., Beers, T. C., & Kim, Y. K. 2019, ApJ, 885, 102,
doi: 10.3847/1538-4357/ab4791

Limberg, G., Rossi, S., Beers, T. C., et al. 2021, ApJ, 907,
10, doi: 10.3847/1538-4357/abcb87

Lindegren, L., Klioner, S. A., Hernández, J., et al. 2021a,
A&A, 649, A2, doi: 10.1051/0004-6361/202039709

Lindegren, L., Bastian, U., Biermann, M., et al. 2021b,
A&A, 649, A4, doi: 10.1051/0004-6361/202039653

Lucchini, S., Pellett, E., D'Onghia, E., & Aguerri, J. A. L.
2022, arXiv e-prints, arXiv:2206.10633.
https://arxiv.org/abs/2206.10633

Mackereth, J. T., Schiavon, R. P., Pfeffer, J., et al. 2019,
MNRAS, 482, 3426, doi: 10.1093/mnras/sty2955

Mahalanobis, P. C. 1936, in On the generalized distance in
statistics, National Institute of Science of India

Maiolino, R., & Mannucci, F. 2019, A&A Rv, 27, 3,
doi: 10.1007/s00159-018-0112-2

Majewski, S. R., Schiavon, R. P., Frinchaboy, P. M., et al.
2017, AJ, 154, 94, doi: 10.3847/1538-3881/aa784d

Mardini, M. K., Frebel, A., Chiti, A., et al. 2022, arXiv
e-prints, arXiv:2206.08459.
https://arxiv.org/abs/2206.08459

McInnes, L., Healy, J., & Astels, S. 2017, The Journal of
Open Source Software, 2, 205

Meingast, S., Alves, J., & Fürnkranz, V. 2019, A&A, 622,
L13, doi: 10.1051/0004-6361/201834950

Miyamoto, M., & Nagai, R. 1975, PASJ, 27, 533

Morrison, H. L. 1990, JRASC, 84, 107

Myeong, G. C., Belokurov, V., Aguado, D. S., et al. 2022,
arXiv e-prints, arXiv:2206.07744.
https://arxiv.org/abs/2206.07744

Myeong, G. C., Evans, N. W., Belokurov, V., Amorisco,
N. C., & Koposov, S. E. 2018, MNRAS, 475, 1537,
doi: 10.1093/mnras/stx3262

Myeong, G. C., Vasiliev, E., Iorio, G., Evans, N. W., &
Belokurov, V. 2019, MNRAS, 488, 1235,
doi: 10.1093/mnras/stz1770

Naidu, R. P., Conroy, C., Bonaca, A., et al. 2020, ApJ, 901,
48, doi: 10.3847/1538-4357/abaef4

Navarro, J. F., Frenk, C. S., & White, S. D. M. 1997, ApJ,
490, 493, doi: 10.1086/304888

Necib, L., Lisanti, M., & Belokurov, V. 2019a, ApJ, 874, 3,
doi: 10.3847/1538-4357/ab095b

Necib, L., Lisanti, M., Garrison-Kimmel, S., et al. 2019b, ApJ, 883, 27, doi: 10.3847/1538-4357/ab3afc

Necib, L., Ostdiek, B., Lisanti, M., et al. 2020a, ApJ, 903, 25, doi: 10.3847/1538-4357/abb814

—. 2020b, Nature Astronomy, 4, 1078, doi: 10.1038/s41550-020-1131-2

Norris, J., Bessell, M. S., & Pickles, A. J. 1985, ApJS, 58, 463, doi: 10.1086/191049

Ostdiek, B., Necib, L., Cohen, T., et al. 2019, Cataloging Accreted Stars within Gaia DR2 Using Deep Learning, Published version, Zenodo, doi: 10.5281/zenodo.3579379

Ostdiek, B., Necib, L., Cohen, T., et al. 2020, A&A, 636, A75, doi: 10.1051/0004-6361/201936866

Price-Whelan, A., Sipcz, B., Starkman, N., et al. 2022, adrn/gala: v1.5, v1.5, Zenodo, doi: 10.5281/zenodo.6325733

Price-Whelan, A. M. 2017, The Journal of Open Source Software, 2, doi: 10.21105/joss.00388

Ramos, P., Antoja, T., & Figueras, F. 2018, A&A, 619, A72, doi: 10.1051/0004-6361/201833494

Re Fiorentin, P., Spagna, A., Lattanzi, M. G., & Cignoni, M. 2020, arXiv e-prints, arXiv:2012.10957. https://arxiv.org/abs/2012.10957

Reid, M. J., & Brunthaler, A. 2004, ApJ, 616, 872, doi: 10.1086/424960

Riello, M., De Angeli, F., Evans, D. W., et al. 2021, A&A, 649, A3, doi: 10.1051/0004-6361/202039587

Ruiz-Lara, T., Matsuno, T., Sofie Lövdal, S., et al. 2022, arXiv e-prints, arXiv:2201.02405. https://arxiv.org/abs/2201.02405

Sanderson, R. E., Wetzel, A., Loebman, S., et al. 2020, ApJS, 246, 6, doi: 10.3847/1538-4365/ab5b9d

Schlaufman, K. C., Rockosi, C. M., Allende Prieto, C., et al. 2009, ApJ, 703, 2177, doi: 10.1088/0004-637X/703/2/2177

Sestito, F., Longeard, N., Martin, N. F., et al. 2019, MNRAS, 484, 2166, doi: 10.1093/mnras/stz043

Shank, D., Beers, T. C., Placco, V. M., et al. 2022, ApJ, 926, 26, doi: 10.3847/1538-4357/ac409a

Smirnov, N. 1948, Ann. Math. Statist., 19, 279, doi: 10.1214/aoms/1177730256

Sofie Lövdal, S., Ruiz-Lara, T., Koppelman, H. H., et al. 2022, arXiv e-prints, arXiv:2201.02404. https://arxiv.org/abs/2201.02404

Soubiran, C., Bienaymé, O., & Siebert, A. 2003, A&A, 398, 141, doi: 10.1051/0004-6361:20021615

Trick, W. H., Coronado, J., & Rix, H.-W. 2019, MNRAS, 484, 3291, doi: 10.1093/mnras/stz209

van der Walt, S., Colbert, S. C., & Varoquaux, G. 2011, Computing in Science Engineering, 13, 22, doi: 10.1109/MCSE.2011.37

Vasiliev, E. 2019, MNRAS, 482, 1525, doi: 10.1093/mnras/sty2672

Wechsler, R. H., & Tinker, J. L. 2018, ARA&A, 56, 435, doi: 10.1146/annurev-astro-081817-051756

Wetzel, A. R., Hopkins, P. F., Kim, J.-h., et al. 2016, ApJL, 827, L23, doi: 10.3847/2041-8205/827/2/L23

White, S. D. M., & Rees, M. J. 1978, MNRAS, 183, 341, doi: 10.1093/mnras/183.3.341

Wolf, C., Onken, C. A., Luvaul, L. C., et al. 2018, PASA, 35, e010, doi: 10.1017/pasa.2018.5

Wu, Y., Valluri, M., Panithanpaisal, N., et al. 2022, MNRAS, 509, 5882, doi: 10.1093/mnras/stab3306

Yang, C., Xue, X.-X., Li, J., et al. 2019, ApJ, 880, 65, doi: 10.3847/1538-4357/ab2462

Zhao, G., Zhao, Y.-H., Chu, Y.-Q., Jing, Y.-P., & Deng, L.-C. 2012, Research in Astronomy and Astrophysics, 12, 723, doi: 10.1088/1674-4527/12/7/002

Zolotov, A., Willman, B., Brooks, A. M., et al. 2009, ApJ, 702, 1058, doi: 10.1088/0004-637X/702/2/1058

APPENDIX

In this appendix, we show the figures associated with the N_{stack} cuts. Fig S1 shows the number of stars associated with any cluster at N_{stack} number of realizations. Figure S2 shows the error distribution of stars with various N_{stack} cuts. We also include Figure S3 and S4, showing the clustering result on the velocity and integrals of motion spaces respectively, without placing any N_{stack} cut on the stacked sample. As expected they include a much larger number of clusters. We also include Figure S5, the equivalent of Figure 7 in integrals of motion space. Finally, Figure S6 shows the resulting clustering, having removed cluster NGC 3201 (see related discussion in Section 5.3).
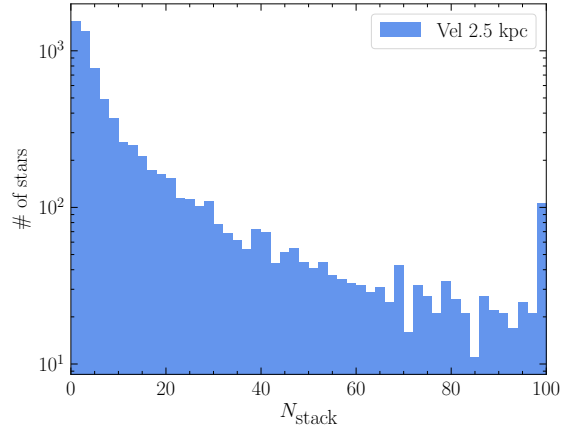
Figure S1. Distribution of N_{stack} for the stacked full subsample with Z_{max} 2σ above 2.5 kpc from the cylindrical velocity space.
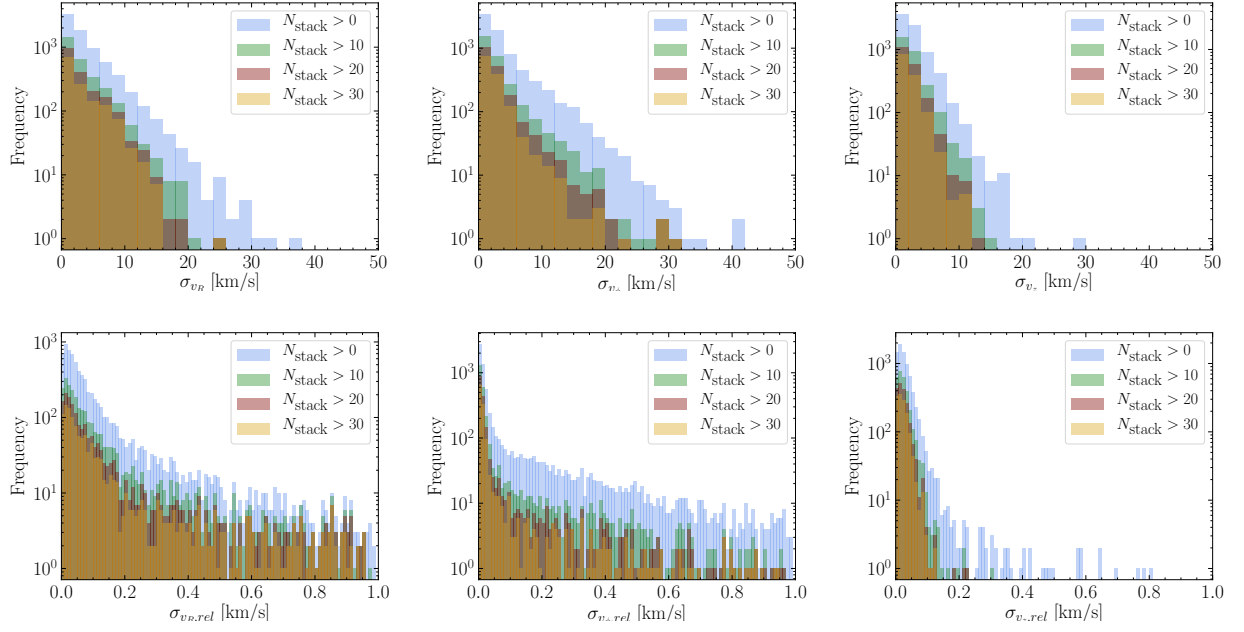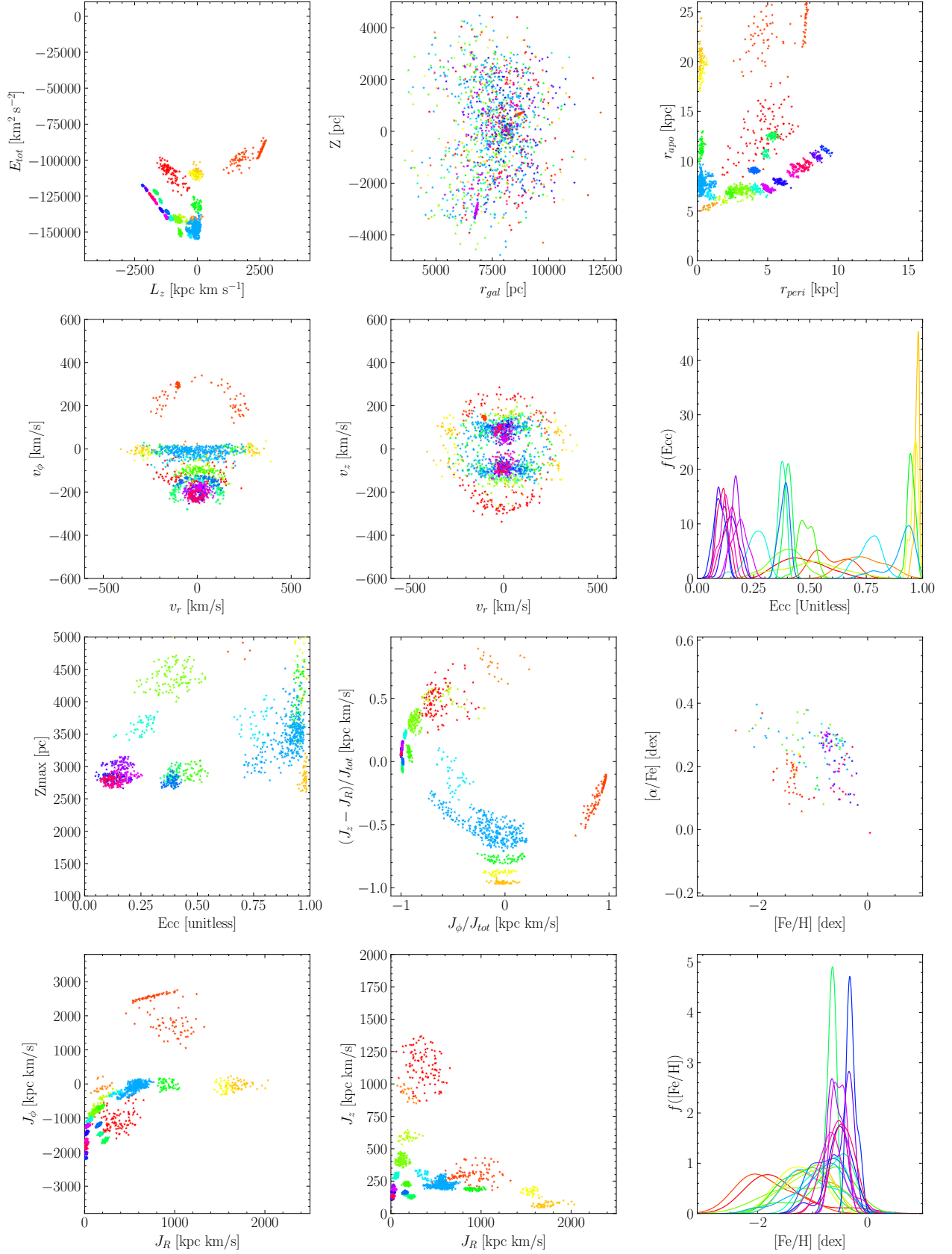
Figure S2. Absolute and relative error distribution of cylindrical velocities for the stacked full subsample with Z_{max} $2\,\sigma$ above 2.5 kpc at different N_{stack} cuts. Note that the y axis is on logarithmic scale.
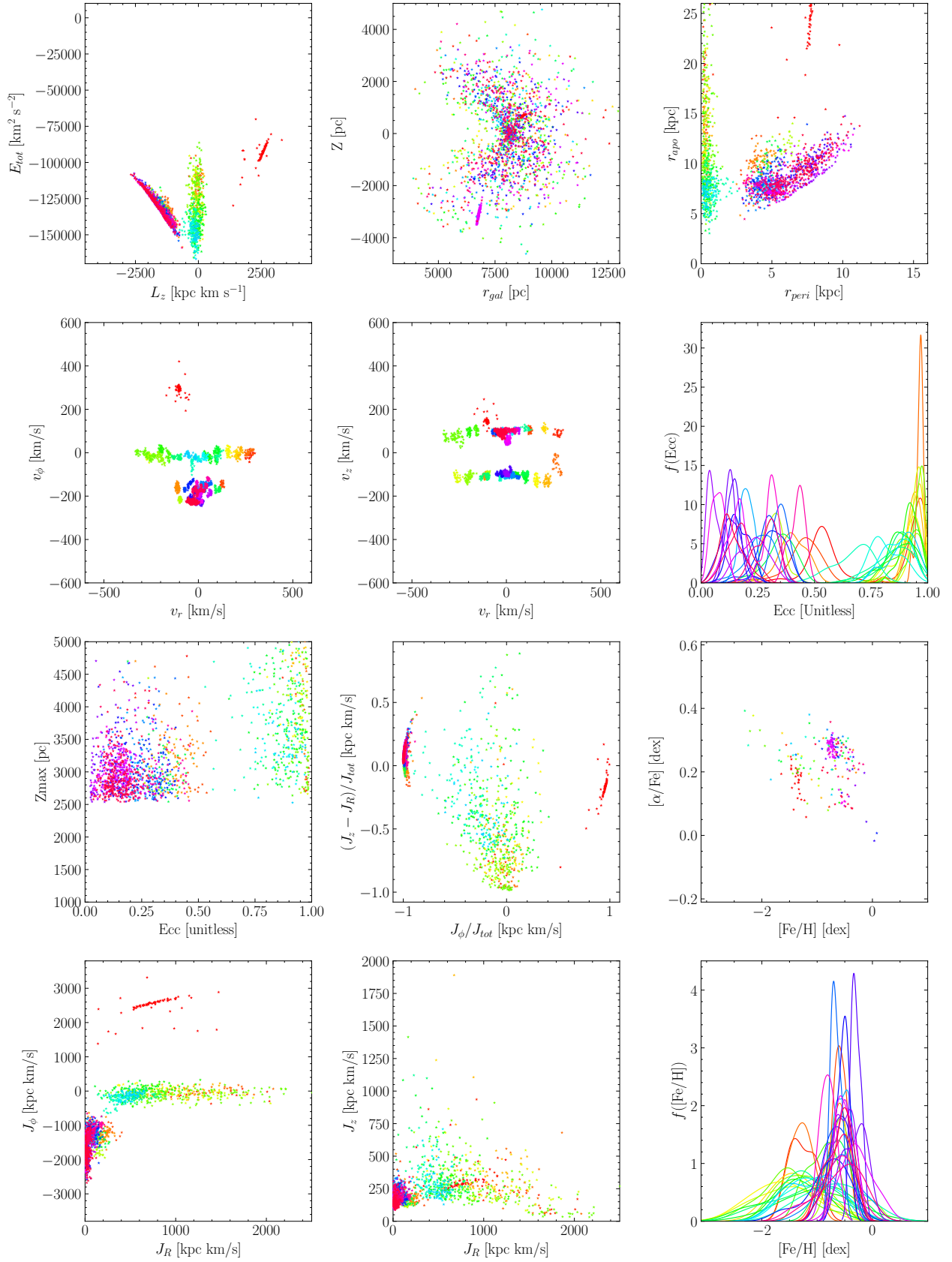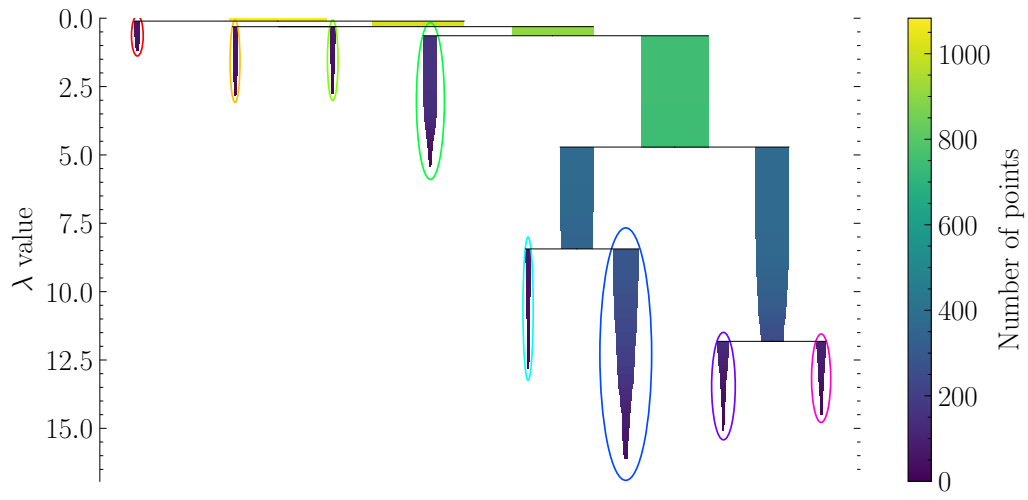
Figure S3. Summary plot for clusters that `HDBSCAN` identified from stacked full subsample with $Z_{\max}$ $2\,\sigma$ above 2.5 kpc from the cylindrical velocity space.
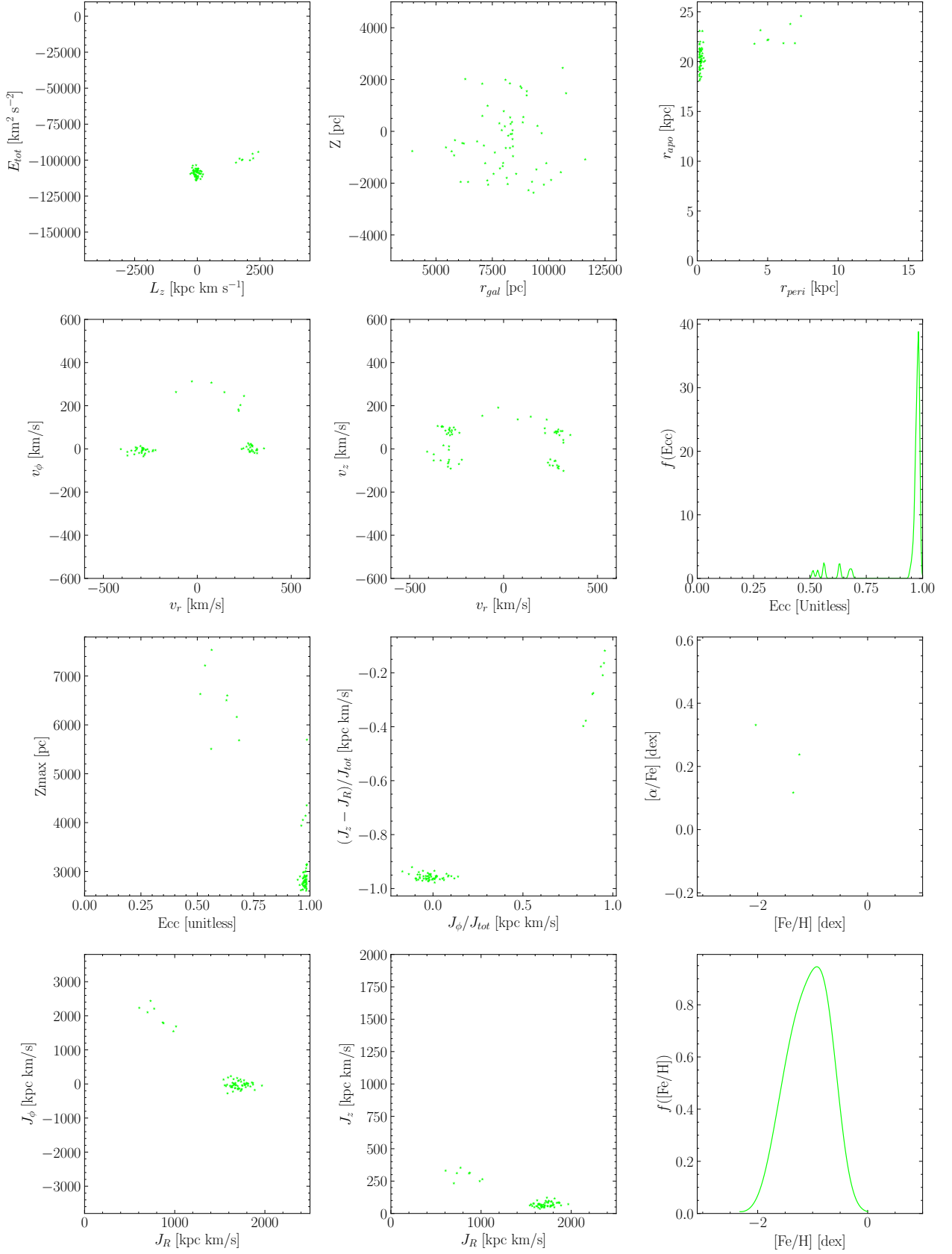
Figure S4. Summary plot for clusters that `HDBSCAN` identified from stacked full subsample with Z_{max} $2\,\sigma$ above 2.5 kpc from the Energy + 3D action space.

Figure S5. Condensed merger tree for the stacked subsample with $N_{\text{stack}} > 20$ and Z_{max} $2\,\sigma$ above 2.5 kpc from the Energy + 3D action space.

Figure S6. Summary plot for cluster 1 from `HDBSCAN` identified from stacked stable ($N_{stack} > 20$) subsample with Z_{max} 2σ above 2.5 kpc from the Energy+Action space with NGC 3201 removed.